Topias Väisänen

SIMULATION OF ELECTROMECHANI-CALLY ACTUATED BOOM

ABSTRACT

Topias Väisänen: Simulation of Electromechanically actuated boom.
Master of Science Thesis
Tampere University
Master's Degree Program in Mechanical Engineering
January 2023

Environmental consciousness has made electrification of mobile machines a popular trend in recent years. Electromechanical linear actuators (EMLAs) may be used to replace hydraulic cylinders in mobile machines. In this thesis a simulation model for a boom with single EMLA is developed. The EMLA consists of a permanent magnet synchronous motor (PMSM), gearbox and ball screw. The objective of this thesis is to develop a simulation model that includes the EMLA, the control system and the mechanical model of the boom. The simulations are carried out in Matlab Simulink environment. The simulation model is validated by comparing simulation results with measurement data of the actual system.

Structure, operating principle, mathematical equations and common control structure of PMSM are introduced to develop a simulation model for the motor and motor controller. The motor used in this thesis uses Hall sensors as feedback device. The downsides and challenges of using such low-resolution sensors are also covered in this thesis. A spring-mass model is used to model the mechanics of the actuator. The equations to obtain parameters for the spring mass models are introduced. Friction of the actuator is also studied, and it is found out that there are no friction models that could predict the friction accurately using basic parameters of the ball-screw. There are many components corresponding to total friction and developing an experimental model is the best option. A simple assumption of constant efficiency of the actuator is used in this thesis.

The simulation model of the motor and motor controller was validated independently of the rest of the system by utilizing a motor test bench. It was found out that the models are sufficiently accurate to be used for complete system modelling, including the EMLA and the boom. The complete model was then developed, and the results were compared with measurement data from the real system. The results showed similarities and the simulator managed to show controllability issues of the real system. The issues were caused by slow control loop frequency and delay in the control loop. To improve the systems performance a motor and a motor controller better suited for motion control applications should be used. It was found out that the simple friction model used is not accurate and a better model should be developed.

Keywords: EMLA, PMSM, Simulation, Electrification

The originality of this thesis has been checked using the Turnitin OriginalityCheck service.

TIIVISTELMÄ

Ympäristötietoisuus on tehnyt työkoneiden sähköistyksestä suositun trendin viimevuosina. Elektromekaanisia lineaariaktuaattoreita (EMLA) voidaan käyttää korvaamaan hydraulisylinterit työkoneissa. Tässä opinnäytetyössä kehitetään simulointimalli puomille, jossa on yksi EMLA. EMLA koostuu kestomagneettimoottorista, vaihdelaatikosta ja kuularuuvista. Tässä opinnäytetyössä kehitetään simulointimalli, joka sisältää EMLA:n, ohjausjärjestelmän ja puomin mekaanisen mallin. Simuloinnit suoritetaan Matlab Simulink -ympäristössä. Simulointimalli validoidaan vertaamalla simulointituloksia mittausdataan oikeasta järjestelmästä.

Kestomagneettimoottorin rakenne, toimintaperiaate ja ohjaustapa esitellään moottorin ja moottorinohjaimen simulointimallin kehittämiseksi. Tässä opinnäytetyössä käsiteltävä moottori käyttää Hall-antureita takaisinkytkentään. Myös tästä matalaresoluutioisesta anturista johtuvia haasteita ja haittapuolia käsitellään. Toimilaitteen mekaniikka mallinnetaan jousi-massa-järjestelmänä. Jousi-massa-malliin tarvittavien parametrien yhtälöt esitellään tässä työssä. Myös toimilaitteen kitkaa tutkitaan ja huomataan, että kuularuuvin kitkalle ei ole olemassa mallia, joka ennustaisi kitkavoiman tarkasti käyttäen kuularuuvin perusparametreja. Toimilaitteen kitka muodostuu monen komponentin yhteisvaikutuksesta ja paras vaihtoehto on käyttää kokeellista mallia. Tässä työssä yksinkertaistetusti oletetaan toimilaitteen hyötysuhteen olevan vakio.

Moottorin ja moottorinohjaimen simulointimalli validoitiin erillään muusta järjestelmästä käyttäen moottoritestipenkkiä. Todettiin, että mallit ovat riittävän tarkkoja käytettäväksi koko järjestelmän mallissa, joka sisältää EMLAn ja puomin. Tämän jälkeen koko järjestelmän simulointimalli kehitettiin ja tuloksia verrattiin mittausdataan. Tulokset olivat samankaltaisia, ja todettiin, että simulointimallissa ilmenee samat ohjattavuusongelmat kuin oikeassakin järjestelmässä. Ongelmat johtuvat hitaasta ohjausloopin taajuudesta ja viiveestä ohjausloopissa. Järjestelmän suorituskyvyn parantamiseksi moottori ja moottorinohjain tulisi vaihtaa paremmin tarkoitukseen sopiviin. Toimilaitteen kitkamalli todettiin epätarkaksi ja parempi malli tulisi kehittää.

Avainsanat: EMLA, sähkösylinteri, kestomagneettimoottori, sähköistys

PREFACE

I would like to express my sincere gratitude to my family and friends who have provided support throughout my studies. Without my fiancée Maiju I would likely still be working on my bachelor's thesis as too many of my friends still do. Beer is responsible for deteorating my grades but on the other hand made this long journey bearable.

Thank you unit of Automation Technology and Mechanical Engineering in Tampere University for providing high-quality education.

Tampere, 27 January 2023

Topias Väisänen

CONTENTS

LIST OF FIGURES

LIST OF SYMBOLS AND ABBREVIATIONS

EMLA	Electromechanical linear actuator
PMSM	Permanent magnet synchronous motor
PM	Permanent magnet
SynRM	Synchronous reluctance motor
PMSynRM	Permanent magnet assisted synchronous reluctance motor
BEMF	Back electro-motive force
PMAC	Permanent magnet AC
BLDC	Brushless DC
IPM	Interior permanent magnet
SPM	Surface permanent magnet
PI	Proportional-integral
MTPA	Maximum torque per ampere
SVPWM	Space vector pulse width modulation
CVCP	Constant voltage constant power
DOF	Degrees of freedom
PID	Proportional integral derivative

1. INTRODUCTION

Environmental consciousness is currently driving many industries to shift from fossil fuels to using electricity as energy source. One major example is passenger electric vehicles whose sales have experienced exponential growth in recent years [1]. Many other industries are also starting to offer electric alternatives to traditional machines and one of them is mobile machinery. For many decades mobile machines have relied on internal combustion engines as prime power source. Hydraulic systems are conventionally used to transmit the power both in rotational and linear motion. In recent years manufacturers have put effort on developing fully electric machines. In 2022 Ponsse launched EV1 electric forest machine [2]. Moreover, in 2022 Sandvik released fully autonomous electric Amelia drill rig [3]. Both machines still rely on hydraulic cylinders to implement linear motion. There are also examples where hydraulic systems are completely replaced by electromechanical systems. In 2022 Bobcat released a fully electric skid-steer loader that uses electromechanical linear actuators (EMLAs) instead of hydraulic cylinders. In 2019 Yanmar released a mini excavator concept machine that also uses EMLAs to move the boom. However, Bobcat's and Yanmar's electric machines are relatively small. Replacing hydraulic cylinders in with EMLAs in larger mobile applications is to be expected as the development continues.

This thesis is part of a project where the hydraulic lift actuator of a mobile machine's boom is replaced with an EMLA. Mass of the boom is over 3000 kg, and the load of the actuator is around 200 kN at its highest. Figure 1 presents simplified interpretation of the boom and the components that are used to replace the hydraulic actuator. The components include the EMLA itself and the controllers that are used to control the actuator. The objective of this thesis is to develop and validate a simulation model of the boom. The simulation model includes model of the electric motor and controller, mechanical model of the EMLA and mechanical model of the boom. Vast amount of information is available about modelling electric drives including books about the topic [4]. Mechanical model of the actuator is also much studied as linear servo mechanisms are used in many industrial applications [5]. The objective in this thesis is to construct a simulation model that is detailed enough to predict controllability of the system.
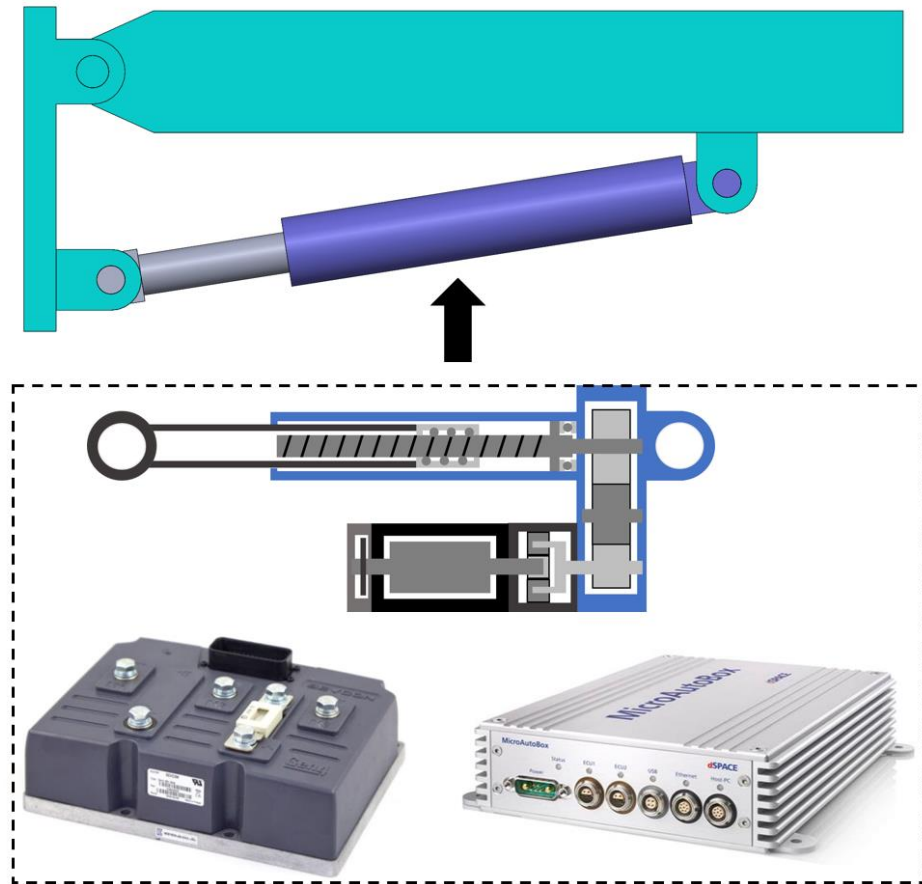
Figure 1.   *Replacing hydraulic actuator with EMLA.*

This thesis consists of six chapters. The second chapter introduces the type of electric motor used in this thesis and the control systems of the motor. Mathematical equations for modelling the motor and the motor controller are presented. The third chapter considers the mechanics of the system including inertia, stiffness and friction. In the fourth chapter simulation model of the electric motor and controller are presented. A motor test bench is constructed to validate the electric drive model independently of the rest of the system. Fifth chapter presents the simulation model of the complete system. The simulation results are compared with measurement data to validate the model. In the final chapter conclusions are presented.

2. PERMANENT MAGNET SYNCHRONOUS MO-TOR

This part of the thesis introduces permanent magnet synchronous motor (PMSM) operating principle and equations for mathematical modelling of the machine. The permanent magnet motor is also briefly compared to other motor types to justify the use of this type of machine.

To develop a simulation model for the PMSM also motor control must be considered. Commonly used methods for PMSM control are studied to simulate a commercial motor controller.

2.1 Brushless PM motor in comparison to other motor types

In electric motors the torque is generated by the interaction of flux from two sources. In permanent magnet (PM) brush motors (also called brush DC motors) field flux is generated by stator magnets and armature flux is generated by rotor windings. The PM brush motor relies on brushes contacting with the commutator attached to the rotor to energize appropriate windings at given rotor position. The mechanical commutation of brush DC motors makes controlling them simple. However, the commutator causes electrical and audible noise, lowers efficiency due to friction and voltage drop, increases the motors size, and is complex to manufacture. Furthermore, the brusher wear producing carbon deposit and require replacing at certain intervals. Low cost of the motor still makes it a valid choice in some low power cost sensitive applications. [6, pp. 313–323] Figure 2 presents the structure of a brushed DC motor.

el. connections   winding   iron core   flange

commutator   permanent magnet housing
(external) (magn. return)

brush system
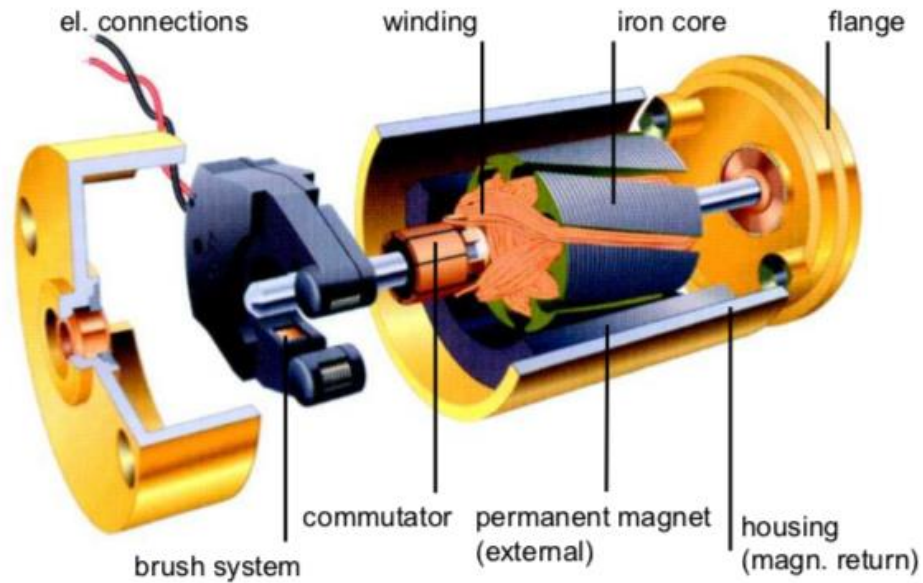
Figure 2.   *Structure of brushed DC motor [7].*

In brushless PM motors the mechanical commutator is replaced by electronic commutation. In brushless PM motor the magnets are located at the rotor and the windings are located at the stator. Brushless PM motors usually have three phases, whereas brush PM motors may have many more. Large number of phases in a brushless PM motor would be impractical since the additional hardware required for additional phases. Rotor of brushless PM motor has significantly lower inertia compared to brushed PM motor making it superior in applications requiring high acceleration. [6, pp. 313–323] In addition, heat is transferred much easier from the windings of a brushless PM motor as the windings are not located in the rotor but in the stator. Together with lower rotor inertia and higher air gap magnetic flux density this makes the brushless motor much smaller in size compared to a brushed motor with similar performance. [8, pp. 14–15] There are also synchronous motors in which the rotor field is produced by windings on the rotor instead of permanent magnets. These machines called synchronous wound rotor motors are used in large power applications [9, pp. 435–436] [10, p. 41].

Another popular motor type is induction motor. Induction motors can be divided to two main types: squirrel cage and wound rotor. In the squirrel cage machine the rotor has longitudinal bars inserted through it. The bars are shorted together at the ends. Wound rotor machines have rotor coils that are connected to collector rings. The rotor circuit is completed with external circuit that is connected to brushes that are in contact with the collector rings. [10, pp. 1–19] The external circuit enables the rotor resistance to be temporarily increased to make better conditions for starting and at operating speed[11, p.

188]. Typically induction motors are of the squirrel cage type.[9, pp. 399–400][12, p. 30] Figure 3 presents the prime difference between the rotors of the two designs.

HIGH STARTING TORQUE

LOW STARTING TORQUE

SLIP RING ROTOR

SQUIRREL CAGE ROTOR
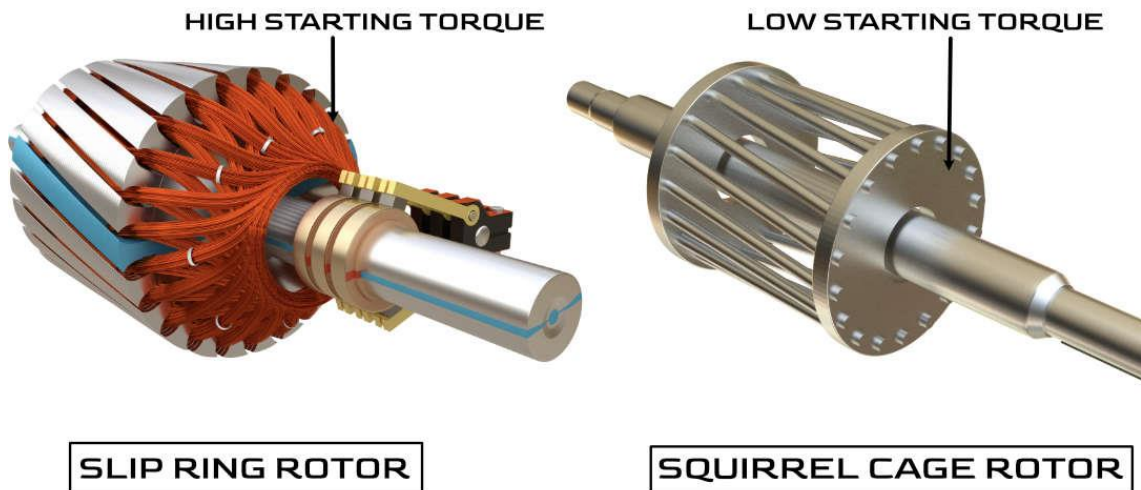
Figure 3.   *Slip ring (wound rotor) and squirrel cage induction motor rotors [13].*

For both types, a rotating magnetic field is generated by stator windings. According to Faraday's and Lenz's laws current is induced in the rotor windings when the speed of the rotor and the stator magnetic field differ [10, pp. 1–19] . Torque is produced when the flux generated by the stator windings interacts with the field generated by rotor currents. The difference in synchronous speed determined by the stator supply voltage frequency and rotor speed is called slipping. [12, p. 33]

PM brushless motors offer higher power density and better dynamic performance than induction motors [8, p. 2][6, p. 339]. Resistive losses are much smaller in brushless PM motor due to absence of rotor current. Higher efficiency and better dynamic performance make the synchronous motor better suited to many applications such as robotics and electric traction. [10, p. 41]

Rare earth permanent magnets provide high efficiency and reduce the size of brushless permanent magnet motors but are also the most expensive active material in the motor [14, p. 9]. Synchronous reluctance motor (SynRM) produces torque utilizing magnetic reluctance. Reluctance in a magnetic circuit is analogous to resistance in an electrical circuit. [6, p. 308] Reluctance torque tries to align the rotor to a position where the flux

created by the stator windings faces least reluctance. SynRM has the advantage of lacking rear earth magnet but does not deliver the same torque density as PMSM motors. Commercial solutions focus mainly on replacing induction motors in industrial applications such as pumps and fans [15, pp. 1–5]. Figure 4 presents ABB's SynRM motor.

Figure 4.   *ABB IE5 synchronous reluctance motor [16].*

Performance of the SynRM can be improved without using rare earth materials by inserting ferrite magnets to the rotor. These machines are called Permanent Magnet assisted Synchronous Reluctance Motor (PMSynRM). [15, pp. 1–6] SynRM and PMSynRM might challenge the PM brushless motors more in the future especially if the use of rare earth magnets becomes less desirable.

2.2   PMSM structure

When effects of stator slots and nonideal winding distribution are disregarded, a balanced three-phase power supply in three-phase stator windings produces a synchronously rotating magnetic field. This is one of the most fundamental principle concerning induction machines and is true for synchronous machines as well [12, pp. 30–74]. The back electro-motive force (BEMF) of a PM machine with sinusoidal winding distribution is also sinusoidal. Feeding the stator windings with balanced three phase currents is called sinusoidal commutation. Sinusoidal commutation of the PM machine is associated with high efficiency and ripple free torque [6, pp. 323–326].

Sinusoidally excited brushless PM motors are referred to as PMSM. They may also be called permanent magnet AC motors (PMAC) motors. There are also PM brushless motors that are fed with rectangular or trapezoidal wave forms. These motors are controlled by energizing only two windings at a time. The current waveform is similar to brush DC motors, and they are often called brushless DC (BLDC) motors. PMSM and BLDC construction is essentially the same [8, pp. 3–13]. BLDC motors are designed for simple six-step switching scheme [10, p. 341]. This six-step commutation is simpler than sinusoidal commutation but doesn't provide as smooth torque [6, p. 336]. BLDC motors may be built with concentrated windings making the machine inexpensive compared to motor with sinusoidally distributed windings. [12, p. 93]

Distributed windings are widely used in brushless PM machines due to more sinusoidal magnetomotive force and BEMF waveforms. However, concentrated windings have gained more attention in 21st century. Concentrated windings can provide shorter winding end turns, higher power density, wider constant power range and better fault tolerance. Some unwanted phenomena including torque ripple and rotor losses pose challenges for concentrated winding designs [17]. Despite the flux density waveform not being sinusoidal it is still possible to achieve smooth torque and sinusoidal BEMF [18]. Performance improvements together with easier manufacturing grow interest in concentrated winding designs especially in high production volume applications [19].

In addition to different winding configurations, there are also many ways to build the rotor of a PMSM. The rotors can be classified as salient and non-salient rotors. Non-salient PM machines produce torque only due to field flux but salient rotor machines also produce reluctance torque [12, p. 485]. Figure 5 presents salient and non-salient rotors. The interior permanent magnet (IPM) rotor is salient, and the surface permanent magnet (SPM) rotor is non-salient. The PMSynRM introduced in 2.1 is very similar to IPM motor; they both produce torque utilizing both PMs and reluctance. The machine is usually referred as IPM when the PM flux is the dominant torque producer [20, p. 28].
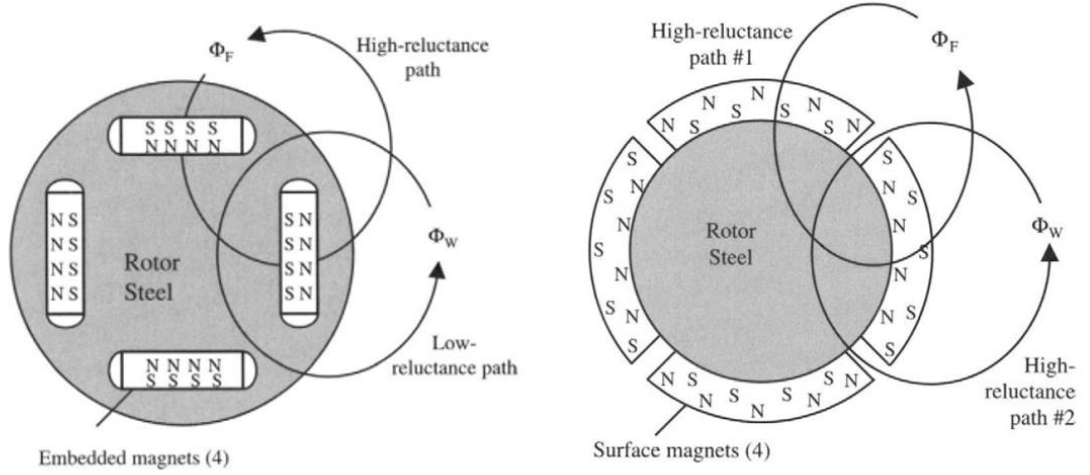
Figure 5. *IPM (left) and SPM (right) rotors. Adopted from [6, p. 330].*

Different winding and rotor configurations make classifying permanent magnet motors complicated. The naming conventions are not always consistent and can cause confusion. Dividing the motors to PMSMs (or PMACs) and BLDCs according to intended phase current waveform seems the best option. This convention distinguishes the concentrated winding motors with sinusoidal excitation from the generally less expensive BLDC motors designed for simple six-step commutation.

2.3 Mathematical model for PMSM

To understand control of PMSM and develop simulation models, the theory of the machine is studied next. Equations describing dynamics of the machine are studied first in stator reference frame and then in reference frame rotating with the rotor. Controlling and simulation of the machine is studied in the rotating reference frame.

2.3.1 PMSM equations in stator reference frame

According to Faraday's and Ohm's laws the electrical dynamics of the machine can be modelled with the following equation [10, p. 46]:

$$\begin{bmatrix} V_a \\ V_b \\ V_c \end{bmatrix} = \begin{bmatrix} R_s & 0 & 0 \\ 0 & R_s & 0 \\ 0 & 0 & R_s \end{bmatrix} \begin{bmatrix} I_a \\ I_b \\ I_c \end{bmatrix} + \frac{d}{dt} \begin{bmatrix} \phi_{sa} \\ \phi_{sb} \\ \phi_{sc} \end{bmatrix}, \tag{2.1}$$

where V_{abc}, R_s, I_{abc}, ϕ_{sabc} are stator voltage, resistance, current and flux. The stator flux is sum of flux produced by stator currents and flux induced by rotor magnets. Stator flux is described by following equation [10, p. 51]:

$$\phi_{sabc} = [L_{ss}][I_{abc}] + [\phi_{rabc}],\tag{2.2}$$

where ϕ_{sabc}, $[L_{ss}]$, $[\phi_{rabc}]$ are stator flux, stator inductance matrix and flux produced by rotor magnets. The stator inductance matrix can be expressed as [10, p. 46]:

$$[L_{ss}] = \begin{bmatrix} L_a & M_{ab} & M_{ac} \\ M_{ba} & L_b & M_{bc} \\ M_{ca} & M_{cb} & L_c \end{bmatrix},\tag{2.3}$$

where inductances denoted by L are self-inductances and inductances denoted by M are mutual inductances. The inductances are functions of rotor angle making them time varying [10, pp. 46–47]. The flux produced by the rotos magnets is expressed as [10, p. 51]:

$$[\phi_{rabc}] = \begin{bmatrix} \phi_r \cos(p\theta) \\ \phi_r \cos\left(p\theta - \dfrac{2\pi}{3}\right) \\ \phi_r \cos\left(p\theta + \dfrac{2\pi}{3}\right) \end{bmatrix},\tag{2.4}$$

where ϕ_r, p, θ are PM flux amplitude, number of motor pole pairs and rotor mechanical angle. Electromagnetic torque developed by the machine is expressed as [10, p. 51]:

$$T_{em} = \frac{1}{2}[I_{abc}]^T \frac{d[L_{ss}]}{d\theta}[I_{abc}] + [I_{abc}]^T \frac{d[\phi_{rabc}]}{d\theta},\tag{2.5}$$

where T_{em} is electromagnetic torque. In order to form models for analysis and develop high-performance control for the motor a transformation is needed to remove dependency on rotor position [21].

2.3.2 PMSM equations in DQ-frame

Clarke matrix is used to project variables from abc-frame to two-coordinate αβ-frame. There are two versions of this matrix of which one preserves the variable's amplitude, and one preserves energy [10, pp. 24–25]. Clarke matrix preserving the variable's amplitude is:

$$[C] = \frac{2}{3}\begin{bmatrix} 1 & \dfrac{-1}{2} & \dfrac{-1}{2} \\ 0 & \dfrac{\sqrt{3}}{2} & -\dfrac{\sqrt{3}}{2} \end{bmatrix}.\tag{2.6}$$

The energy preserving version of the Clarke matrix is:

$$[C^*] = \sqrt{\frac{2}{3}} \begin{bmatrix} 1 & \dfrac{-1}{2} & \dfrac{-1}{2} \\ 0 & \dfrac{\sqrt{3}}{2} & -\dfrac{\sqrt{3}}{2} \end{bmatrix}. \tag{2.7}$$

Park transformation can then be used to covert from αβ-frame to rotating dq-frame. Park transformation matrix is:

$$[P(\theta)] = \begin{bmatrix} \cos(\theta) & \sin(\theta) \\ -\sin(\theta) & \cos(\theta) \end{bmatrix}, \tag{2.8}$$

where θ is the angular position of the rotating reference frame. [10, pp. 24–45] The amplitude invariant transformation matrix from stator abc-frame to rotor dq-reference frame is:

$$[T_{dq}] = [P(\theta)][C] = \frac{2}{3} \begin{bmatrix} \cos(\theta) & \cos\left(\theta - \dfrac{2\pi}{3}\right) & \cos\left(\theta + \dfrac{2\pi}{3}\right) \\ -\sin(\theta) & -\sin\left(\theta - \dfrac{2\pi}{3}\right) & -\sin\left(\theta + \dfrac{2\pi}{3}\right) \end{bmatrix}. \tag{2.9}$$

The inverse of this transformation is used to transform from dq-frame to abc-frame. The matrix for inverse transformation is:

$$[T_{abc}] = \begin{bmatrix} \cos(\theta) & -\sin(\theta) \\ \cos\left(\theta - \dfrac{2\pi}{3}\right) & -\sin\left(\theta - \dfrac{2\pi}{3}\right) \\ \cos\left(\theta + \dfrac{2\pi}{3}\right) & -\sin\left(\theta + \dfrac{2\pi}{3}\right) \end{bmatrix}. \tag{2.10}$$

The amplitude invariant transformation from abc-frame to dq-frame and the other way are the following:

$$\begin{bmatrix} x_d \\ x_q \end{bmatrix} = [T_{dq}] \begin{bmatrix} x_a \\ x_b \\ x_c \end{bmatrix}, \tag{2.11}$$

$$\begin{bmatrix} x_a \\ x_b \\ x_c \end{bmatrix} = [T_{abc}] \begin{bmatrix} x_d \\ x_q \end{bmatrix}. \tag{2.12}$$

The variables can present currents, voltages or magnetic fluxes [10, p. 44]. Figure 6 presents the balanced sinusoidal currents and the corresponding signals in αβ-frame and dq-frame.
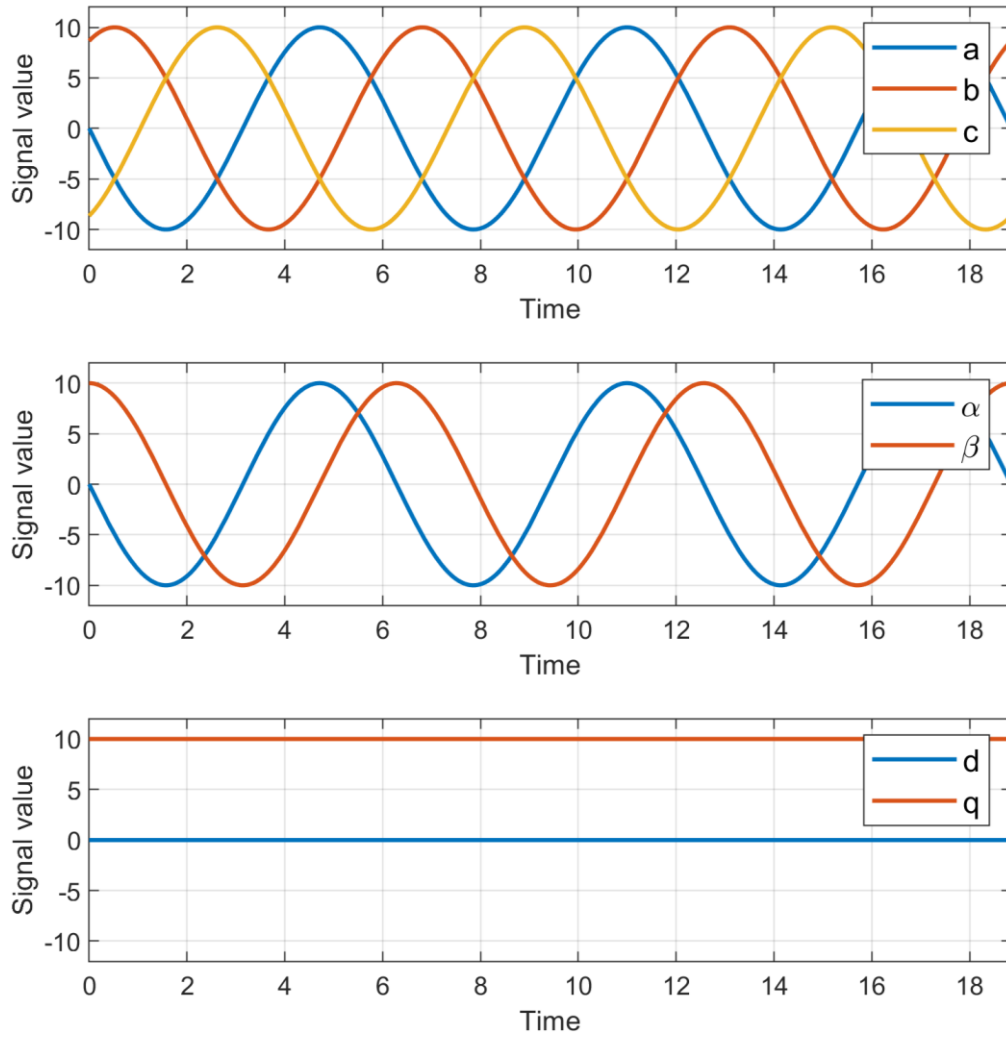
Figure 6. *abc, αβ and dq signals.*

The PMSM voltage equations in dq-frame are expressed as [12, pp. 90–91]:

$$V_d = R_s I_d + L_d \frac{dI_d}{dt} - \omega_e I_q L_q, \tag{2.13}$$

$$V_q = R_s I_q + L_q \frac{dI_q}{dt} + \omega_e \left(I_d L_d + \lambda_{pm} \right), \tag{2.14}$$

where R_s is stator phase resistance, ω_e is motor electrical rotational speed, and V_d, V_q, I_d, I_q, L_d, L_q are d- and q-axis voltages, currents, and inductances. The angular electrical velocity of the motor is expressed as:

$$\omega_e = N\omega_m, \tag{2.15}$$

where *N* is number of pole pairs and ω_m is mechanical rotational speed of the rotor. The electromagnetic torque produced by the machine is expressed as [12, p. 91]:

$$T_e = \frac{3}{2} N(I_q \lambda_{pm} + I_d I_q (L_d - L_q)),\qquad\qquad(2.16)$$

where T_e is electromagnetic torque. Derivation of PMSM equations in dq-frame is not considered in this thesis but the readers particularly interested in this topic may read [12], [22] and [23]. It should be also mentioned that certain assumptions are made when modelling PMSM machines. In [22, p. 54] the presented assumptions are:

- When concerning rotor and stator mutual effects, the windings can be assumed sinusoidally distributed

- Inductance variations with rotor position caused by stator slots are insignificant

- Negligible magnetic hysteresis

- Negligible magnetic saturation.

The first assumption isn't true for all PM machines as some concentrated winding machines have trapezoidal BEMF wave form (BLDC). However, it is possible to design a PMSM with concentrated windings that has nearly sinusoidal BEMF wave form [24]. In [25] dq-equations were applied to PMSM with concentrated windings successfully. The effects of magnetic saturation cannot be neglected in all situations as the inductances varying with current can affect control performance [26].

2.4   Control of PMSM

Figure 7 presents typical structure of PMSM current control in dq-frame. Reference currents I_d^* and I_q^* coming from an outer control loop are compared to measured currents to form reference voltages for the inverter. The inverter produces the phase voltages, and the phase currents are measured for feedback. Measuring only two currents is adequate since the sum of the balanced currents is zero. Rotor position feedback is needed to implement reference frame conversions and to measure speed.
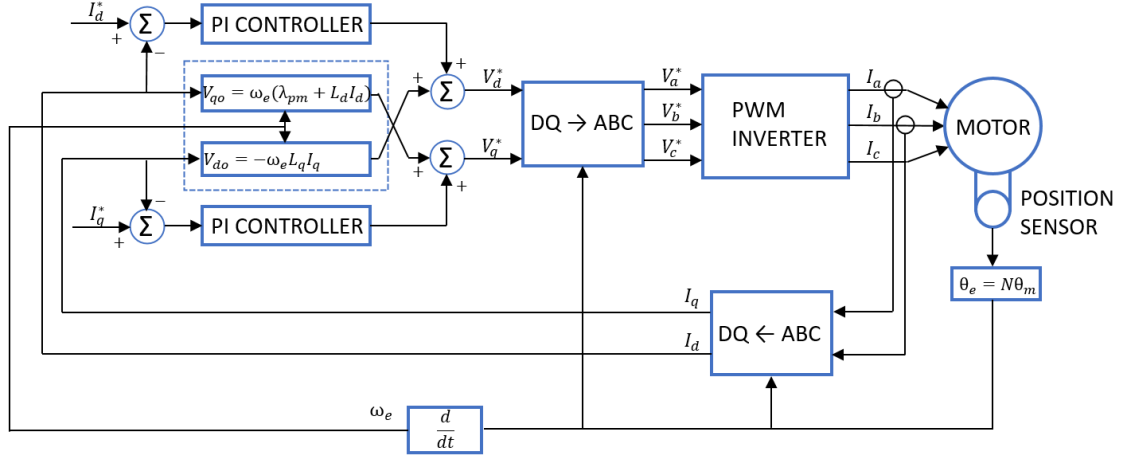
Figure 7. *PMSM current control. Adopted from [4, p. 148].*

Proportional-integral (PI) controllers are widely used for synchronous motor current control [27],[28, p. 153]. Other types of solutions for current control such as flux-based controllers and model predictive controllers exist, but only PI current control will be discussed in this thesis since it is the most common option [29]. From Eqs. (2.13) and (2.14) it can be noted that the currents can't be controlled independently due to cross-coupling. The cross-coupling effect increases with speed. However, the current controller may be equipped with feedforward terms to cancel the cross-coupling effect [30],[27],[4, p. 148]. In figure 6 the feedforward terms are enclosed by a dashed line.

2.4.1 Control of IPM motors

To minimize copper losses (resistive losses in stator windings) the outer control loop should control I_d^* and I_q^* so that the required torque is produced with smallest current possible. This is called maximum torque per ampere (MTPA) control [31]. From Eq. (2.16) two terms producing torque can be identified: term $I_q\lambda_{pm}$ producing magnet excitation torque and the term $I_dI_q(L_d - L_q)$ producing reluctance torque. IPM motors' d-axis inductance is smaller than q-axis inductance. The term $L_d - L_q$ in Eq. (2.16) becomes negative and torque production is increased with negative d-axis current. To solve the optimal combination of I_d and I_q they can be expressed as [31]:

$$I_d = -I_s sin\beta, \tag{2.17}$$

$$I_q = I_s cos\beta, \tag{2.18}$$

where I_s the amplitude of stator current and β is current phase angle. By substituting Eqs. (2.17) and (2.18) to Eq. (2.16) one obtains:

$$T_e = \frac{3}{2}N\left(I_s cos\beta\lambda_{pm} - I_s^2 cos\beta sin\beta(L_d - L_q)\right).$$

(2.19)

From Eq. (2.19) the magnetic excitation torque is distinguished as $\frac{3}{2}NI_s cos\beta\lambda_{pm}$ and reluctance torque as $-\frac{3}{2}NI_s^2 cos\beta sin\beta(L_d - L_q)$. Parameters of laboratory IPM motor used in [30] are also used in this thesis for IPM analysis. The parameters are presented in table 1.

Table 1.   Parameters of IPM motor.

Number of pole pairs	2
Phase resistance	0.57 Ω
PM flux-linkage	0.108 Wb
d-axis inductance	8.72 mH
q-axis inductance	22.8 mH
Maximum phase voltage	50 V
Maximum phase current	8.66 A

Figure 8 presents total torque, magnet excitation torque and reluctance torque of IPM motor as function of phase angle for given I_s.
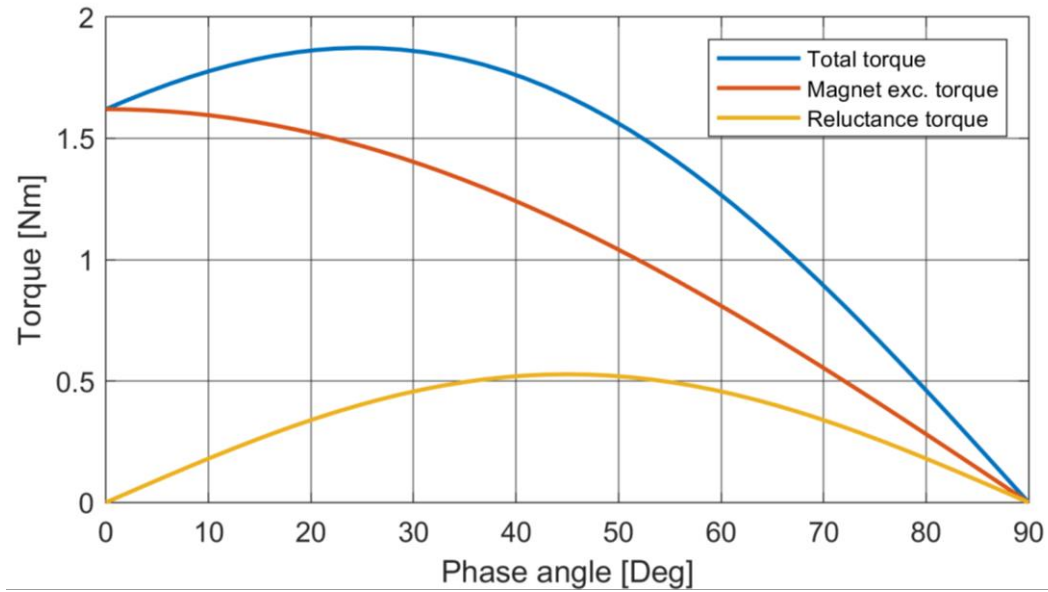
Figure 8. *Torque as function of phase angle.*

By differentiating Eq. (2.19) with respect to β and setting the result to zero the optimal phase angle for maximum total torque can be found.

$$\frac{dT_e}{d\beta} = \frac{3}{2}N\left(-I_s sin\beta\lambda_{pm} - I_s^2(\cos(\beta)^2 - \sin(\beta)^2)\left(L_d - L_q\right)\right) = 0. \qquad (2.20)$$

Optimal I_d as function of I_q for MTPA control is obtained by substituting Eqs. (2.17) and (2.18) to Eq. (2.20) and solving for I_d. Two solutions are found of which one is useful for positive I_q values:

$$I_d = \frac{\lambda_{pm}}{2\left(L_q - L_d\right)} - \sqrt{\frac{\lambda_{pm}^2}{4\left(L_q - L_d\right)^2} + I_q^2}. \qquad (2.21)$$

The outer control loop may control I_q according to torque demand and use Eq. (2.21) to control I_d. MTPA control is relatively simple, but it does not utilize the whole speed range of the motor. To study MTPA control limits and to understand more complicated control methods the limits of the motor and inverted must be recognized.

The maximum current is limited by either the motor or the inverter. The phase current amplitude is related to dq -currents as [6, p. 335]:

$$I_a = \sqrt{I_d^2 + I_q^2}. \qquad (2.22)$$

Maximum torque is produced when the MTPA trajectory defined by (2.21) and the current limiting circle defined by (2.24) cross. The corresponding currents I_{da} and I_{qa} are obtained from (2.21), (2.22) and $I_a = I_{ph,m}$:

$$I_{da} = \frac{\lambda_{pm}}{4(L_q - L_d)} - \sqrt{\frac{\lambda_{pm}^2}{16(L_q - L_d)^2} + \frac{I_{ph,m}^2}{2}}, \qquad (2.23)$$

$$I_{qa} = \sqrt{I_{ph,m}^2 - I_{da}^2}, \qquad (2.24)$$

where $I_{ph,m}$ is the maximum phase voltage limited by the inverter or the motor.

The maximum phase voltage provided by the inverter is limited and depends on the used modulation technique. For space vector pulse width modulation (SVPWM) the maximum phase voltage is [4, p. 128] [28, p. 27]:

$$V_{ph,m} = \frac{V_{DC}}{\sqrt{3}}. \qquad (2.25)$$

In steady state operation the motor voltage Eqs. (2.13) and (2.14) can be written as:

$$V_d = R_s I_d - \omega_e I_q L_q, \qquad (2.26)$$

$$V_q = R_s I_q + \omega_e (I_d L_d + \lambda_{pm}), \qquad (2.27)$$

The phase voltage amplitude is related to dq-voltages as [12, p. 62]:

$$V_a = \sqrt{V_d^2 + V_q^2}. \qquad (2.28)$$

From Eqs. (2.25 – 2.28) it is obvious that the stator voltage increases as the motor speed increases. When the BEMF produced by the motor is equal to inverter DC voltage there is no voltage difference left to drive current. The maximum speed of a loaded motor is lower since the current produces a voltage drop. Looking at Eqs. (2.26) and (2.27) it is noted that with negative I_d values the motor speed range is extended by attaining lower stator voltage magnitude. The air gap flux produced by the permanent magnets is weakened due to demagnetizing effect [30]. Reducing the flux essentially reduces the BEMF produced by the motor and allows operation at higher speeds [6, p. 328]. This technique is referred to as field weakening or flux weakening [6, p. 327],[30]. MTPA control for IPM motors includes some negative I_d but more is needed to use full potential of the motor. From the voltage equations it can be noted that large inductance is favorable for flux weakening operation. IPM motors have good flux weakening characteristics due to relatively large inductance [31],[30]

Including the resistance of the windings would yield long expressions. To simplify the flux weakening analysis, the resistance in voltage Eqs. (2.13) and (2.14) may be neglected and instead consider it in the voltage limitation [30]:

$$V_o = \sqrt{V_{do}^2 + V_{qo}^2} \leq V_{om},$$ (2.29)

where V_o is phase voltage in steady state when resistance is neglected $V_{do} = -\omega_e I_q L_q$, $V_{qo} = \omega_e (I_d L_d + \lambda_{pm})$ and $V_{om} = V_{ph,m} - R_s I_{ph,m}$. Now by setting $V_o = V_{om}$ and solving the equation for I_d one obtains:

$$I_d = \frac{-\lambda_{pm}}{L_d} \pm \frac{1}{L_d} \sqrt{\frac{V_{om}^2}{\omega_e^2} - (I_q L_q)^2}.$$ (2.30)

The result is a voltage limiting ellipse whose size depends on the motor speed. Because the maximum resistive voltage drop is considered in V_{om}, the voltage limitation is always fulfilled in steady state by using Eq. (2.30). Once the motor speed exceeds a certain limit, the point (I_{da}, I_{qa}) where maximum torque is produced lies outside the voltage limiting ellipse. This speed is called the base speed ω_b and can be obtained by solving Eq. (2.30) for ω_e:

$$\omega_b = \frac{V_{om}}{\sqrt{(\lambda_{pm} + I_{da} L_d)^2 + (I_{qa} L_q)^2}}.$$ (2.31)

Figure 9 presents the MTPA trajectory, current limiting circle and voltage limiting ellipses. The MTPA trajectory crosses current limiting circle at point (I_{da}, I_{qa}). The voltage limiting ellipse for base speed also crosses this point. The center of the ellipse remains the same, but the ellipse gets smaller as the speed increases.
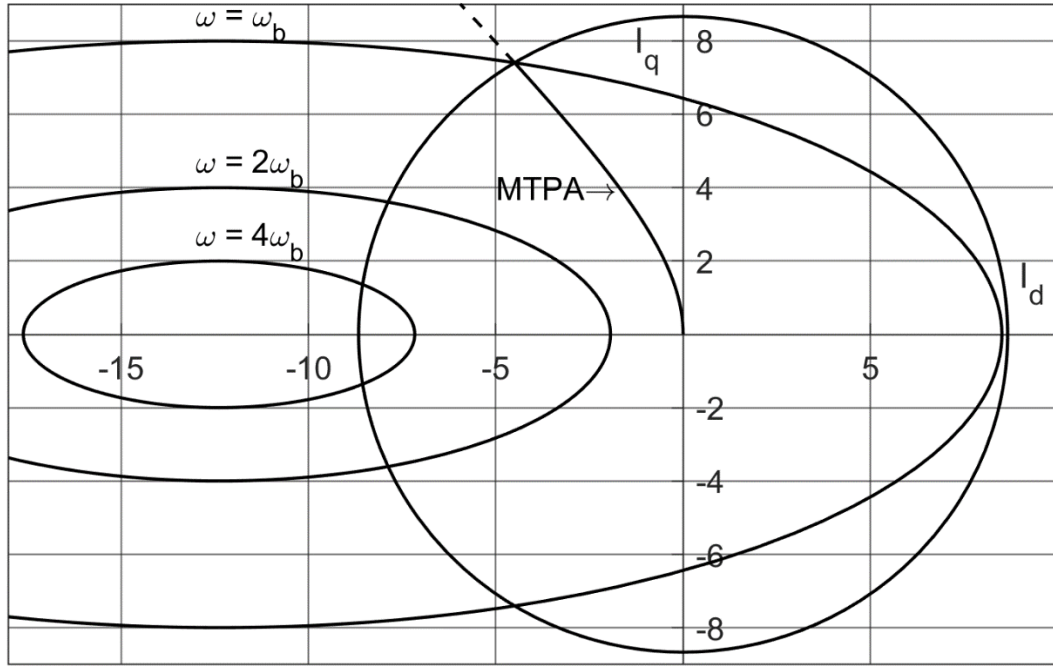
Figure 9. *MTPA trajectory, current limiting circle and voltage limiting ellipses.*

The center of the ellipse is located at point ($I_d = \frac{-\lambda_{pm}}{L_d}$, $I_q = 0$). As the motor speed increases the ellipse essentially becomes a point in the axis I_d. If $I_{ph,m} \geq \frac{\lambda_{pm}}{L_d}$, the point is located inside the current limiting circle, and the theoretical speed of a lossless motor becomes infinite. $\frac{\lambda_{pm}}{L_d}$ is defined as characteristic current [17].

As the motor's speed exceeds the base speed, an algorithm is needed to control the currents in the flux weakening region. The currents must not violate the current limiting circle and the speed dependent voltage limiting ellipse. Maximum power in the flux weakening region for certain speed is produced at the crossing of current limiting circle and voltage limiting ellipse. In [30] it is proposed that reference I_d is calculated based on reference I_q coming from an outer control loop (e.g. speed regulator). In MTPA control mode Eq. (2.21) is used and in flux weakening control mode Eq. (2.30) is used for calculating I_d. Controlling I_d according to voltage limiting ellipse Eq. (2.30) guarantees that including the resistance drop the voltage limit is not violated in steady state. The operation mode (MTPA or flux weakening) is selected by checking whether MTPA control fulfils voltage limitation Eq. (2.29). Under the base speed MTPA control is always selected.

Since the voltage command follows the voltage limiting ellipse in the flux weakening control mode, the voltage is almost equal to the maximum phase voltage provided by the inverter. In transient operation the voltage command from the current controller can

sometimes exceed the maximum phase voltage. When this occurs, the current controllers saturate, and the response becomes worse. In [30] a voltage command compensator was also introduced to overcome this problem. The voltage commands provided by the current controller are manipulated so that I_d is favoured over I_q. A simplified version of algorithm proposed in [30] is presented in Fig. 10.
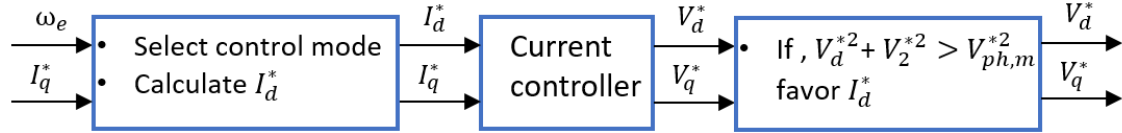
Figure 10. *Structure of current control equipped with flux weakening control.*

It is important to note that here torque isn't directly proportional to I_q, which is the reason this type of control is called indirect torque control [31]. Indirect torque control might be inappropriate for some applications where knowing the magnitude of the torque is important. However, it would be possible to form equations for selecting control mode and current references according to torque demand.

The described flux weakening algorithm can be considered a feed-forward or model-based algorithm since it is based on analytical model of the motor. Feed-forward algorithms perform well in transient operation and have fast response. The downside is that they rely on motor parameters that change with operating conditions. [29] Figure 11 presents prototype IPM motors' experimented d- and q-axis inductances as functions of currents. It can be noted that q-axis inductance is heavily dependent on the q-axis current. This is due to magnetic saturation. If L_q is assumed constant, the response might go unstable as the current controllers saturate in the flux weakening region. [26] In addition, the resistance of the stator windings varies in different operating conditions. The temperature coefficient of resistance for copper is about 0.004/K [32]. This means that the resistance of a winding heated from 20 º C to 100 º C rises about 50 %.
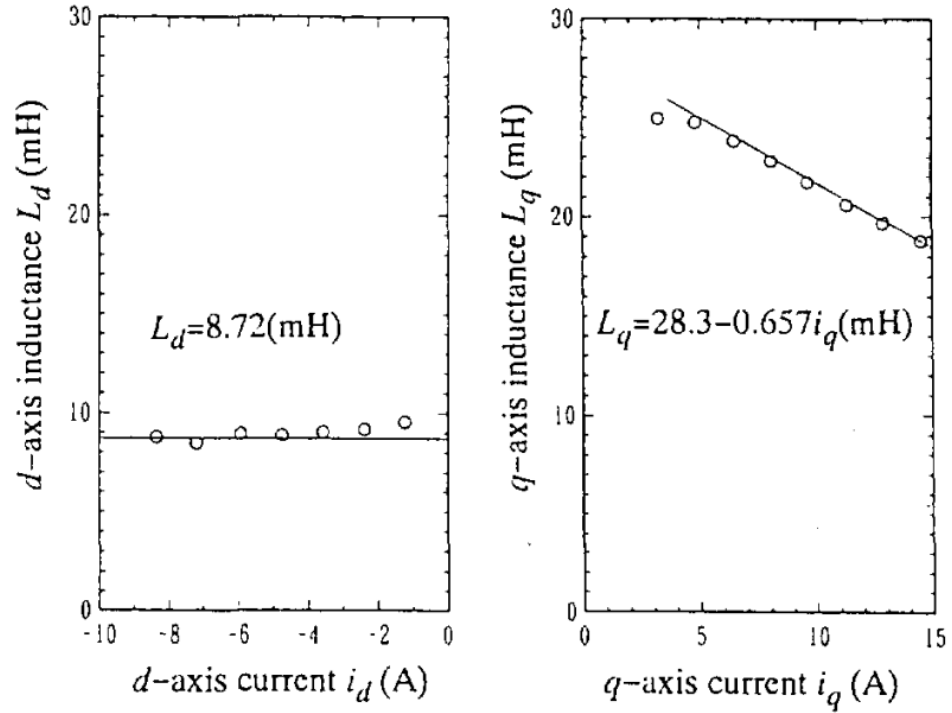
Figure 11. *Prototype IPM motor inductances as functions of currents. [26]*

Research to overcome problems caused by parameter variation has been done in the last few decades. Especially the inductive and resistive parameters have been studied. It is possible to estimate the motor parameters online or use predefined parameters stored in lookup tables. [29] However, to obtain the parameters for e.g., lookup tables, extensive testing of the system is needed. In [26] q-axis inductance was expressed as function of q-axis current based on measured values. The compensated q-axis inductance was used in calculation of reference I_d, in the current controller feedforward term and in the voltage command compensation. Test result showed that by using the compensated value for q-axis inductance, the response in flux weakening region was much more stable.

In addition to feed-forward algorithms also feedback based solutions for flux weakening have been developed. Instead of relying on analytical model of the motor, the inverter reference voltage is used as feedback to regulate the flux weakening. The benefit is the robustness against parameter variation, but the feedback loop introduces delay, and tuning of the control parameters is not trivial. In addition, hybrid solutions combining feedback and feedforward algorithms exist. [29]

2.4.2 Control of SPM motors

For non-salient motors (surface PM motors) the direct and quadrature axes inductances are equal and the machine produces no reluctance torque [12, p. 89]. By setting $L_d = L_q = L$, the torque Eq. (2.16) becomes:

$$T_e = \frac{3}{2} N I_q \lambda_{pm}. \tag{2.32}$$

Electromagnetic torque is proportional to current I_q. This makes MTPA control for SPM motors simple. Current I_q is adjusted according to torque demand and current I_d is kept at zero as it produces no torque. Keeping current I_d at zero minimizes copper losses (resistive losses in stator windings). Since in MTPA region current I_d is kept zero, the maximum torque is produced at point ($I_{da} = 0$, $I_{qa} = I_{ph,m}$).

SPM machines have been considered to have poor flux weakening performance due to relatively low inductance. However, the concentrated winding SPM machines which have gained more interest in the recent years have changed this [17]. By setting $L_d = L_q = L$, the voltage limiting ellipse Eq. (2.30) becomes a circle:

$$I_d = \frac{-\lambda_{pm}}{L} \pm \sqrt{\frac{V_{om}^2}{(\omega_e L)^2} - I_q^2}. \tag{2.33}$$

The base speed ω_b can be obtained by substituting the maximum torque point to Eq. (2.33) and by solving for ω_e:

$$\omega_b = \frac{V_{om}}{\sqrt{\lambda_{pm}^2 + (I_{qa}L)^2}}. \tag{2.34}$$

Similar model-based algorithm can be used for SPM motors as for IPM motors. MTPA control is always preferred, but in speeds greater than the base speed flux weakening is used if necessary. In MTPA control mode I_d is zero and I_q can be determined directly from torque reference according to Eq. (2.32). In flux weakening mode Eq. (2.33) can be used to guarantee that the voltage limitation is fulfilled at least in steady state operation.

In section 2.3.5 it was stated that by neglecting the resistive voltage drop in motor voltage equations and instead taking it into account in maximum phase voltage the analysis is simplified. Since for SPM motors $L_d = L_q = L$, the equations become simpler and including the resistance in motor voltage equations is more feasible. However, in [33] it was

shown that even for SPM motors including the resistance increases complexity of the equation significantly. It was also shown that if the resistance is included in the motor voltage equations, the center of the voltage limiting circle becomes speed dependent. The center of the voltage limiting circle is no longer on the axis I_d. This means that voltage limitation is different for motoring and breaking operation. While in motoring operation the resistive voltage drop limits the voltage that can be used to drive current, in breaking operation the resistive voltage drop allows more torque to be produced before the voltage limitation is exceeded.

To analyze the effect of the resistive voltage drop three different methods are compared: taking the resistance into account, compensating the maximum phase voltage for resistive voltage drop and neglecting the resistance. When the resistance is considered, the voltage limitation is:

$$\sqrt{V_d^2 + V_q^2} \leq V_{ph,m},$$
(2.35)

where $V_d = R_s I_d - \omega_e I_q L_q$ and $V_q = R_s I_q + \omega_e (I_d L_d + \lambda_{pm})$. When the phase voltage is compensated for the resistive voltage drop the voltage limitation is as earlier:

$$\sqrt{V_{do}^2 + V_{qo}^2} \leq V_{om},$$
(2.36)

where $V_{do} = -\omega_e I_q L_q$, $V_{qo} = \omega_e (I_d L_d + \lambda_{pm})$ and $V_{om} = V_{ph,m} - R_s I_{ph,m}$. If the resistance is completely neglected the voltage limitation is:

$$\sqrt{V_{do}^2 + V_{qo}^2} \leq V_{ph,m},$$
(2.37)

where $V_{do} = -\omega_e I_q L_q$ and $V_{qo} = \omega_e (I_d L_d + \lambda_{pm})$. Figure 12 presents the voltage limiting circles for a SPM motor according to Eqs. (2.35-2.37). In addition, MTPA trajectory and current limiting circle is shown. The voltage limiting circles are presented at the base speed and at speed twice the base speed. The base speed is solved from Eq. (2.35) and the same base speed is used for all plots.
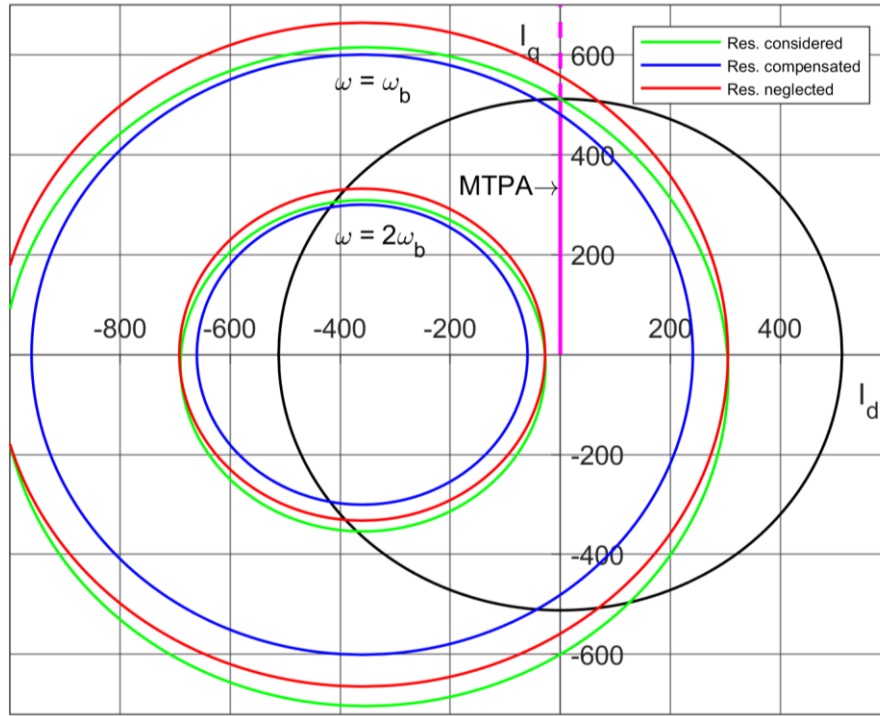
Figure 12. *Voltage limiting circles for SPM motor.*

Following findings can be made from figure 12:

- Only the green plot crosses the current limiting circle and MTPA trajectory at the same point. In other words, the theoretical base speed is higher if resistance is neglected and lower if it is compensated.

- In motoring operation (positive I_q) the red plot is always outside the green plot. Obviously neglecting the resistance does not fulfil the actual voltage limitation.

- In breaking operation (negative I_q) the red plot is inside the green plot. This means that in breaking operation neglecting the resistance in fact is conservative.

- The blue plot is always inside green plot. This means that compensating the maximum phase voltage for maximum resistive voltage drop effectively fulfils the actual voltage limitation.

- The green plots center lies beneath the axis I_d. The voltage limitation is different for motoring and braking operation.

The parameters of the motor used for SPM analysis are presented in table 2. The resistance is quite small which is why the center of the green voltage limiting circle in figure 11 shifts relatively little with speed. High power motors typically have low stator resistance and thus taking it into account is less significant [33].

Table 2.   Parameters of SPM motor.

Number of pole pairs	4
Phase resistance	0.009 Ω
PM flux-linkage	0.0288 Wb
Phase inductance	0.08 mH
DC bus voltage	96 V
Maximum phase current	509.1 A

Figure 13 presents the theoretical maximum power current trajectory. At speeds below the base speed maximum power is produced at point 1 where $I_d = 0$ and $I_q = I_{ph,m}$. As the speed increases above the base speed the voltage limiting circle starts to limit available torque. From point 1 to point 2 the current trajectory follows the intersection of the current limiting circle and the voltage limiting circle. In point 2 the maxima of the voltage limiting circle intersects with the current limiting circle. From point 2 to point 3 the trajectory follows the maxima of the voltage limiting circle. The expressions for plotting figure 12 are quite long and point 2 was solved numerically. The trajectory from point 2 to point 3 is not a vertical line as the I_d coordinate of the voltage limiting circle also shifts with speed when resistance is considered. If Eq. (2.36) or Eq. (2.37) is used for defining the trajectory the expressions are more favorable. It should be noted that if the characteristic current of the motor was larger than the maximum phase current, the trajectory from point 2 to point 3 would be different as the center of the voltage limiting circle would be outside the current limiting circle. Instead of following the maxima of the voltage limiting circle the trajectory would follow the intersection of the circles. The theoretical maximum speed would be the highest speed where the circles intersect.
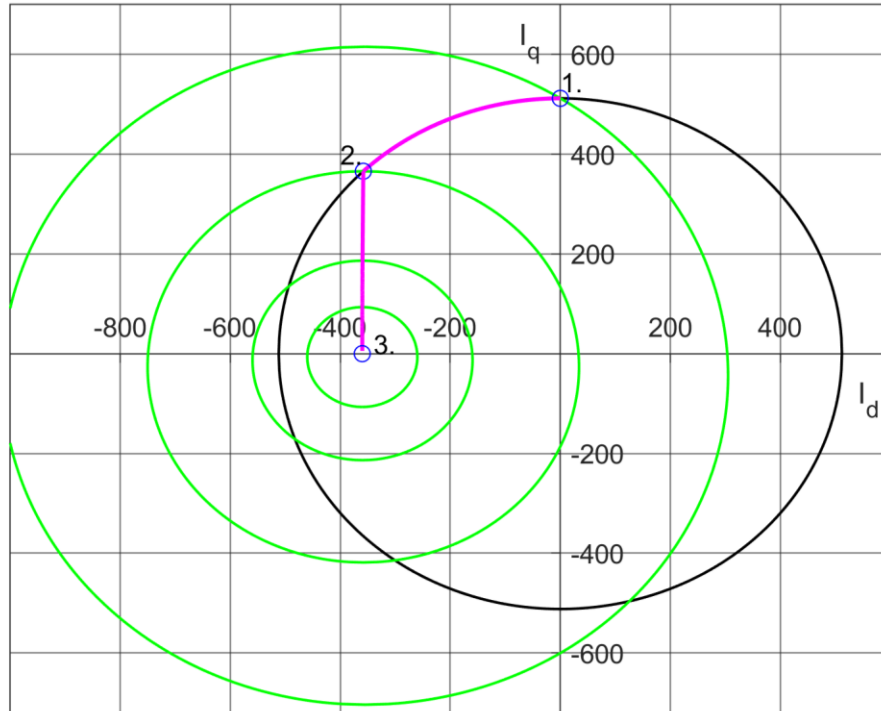
Figure 13. *Theoretical maximum power trajectory.*

Figure 14 presents theoretical maximum torque and power using the optimal current trajectory of figure 13. The results are also shown for the cases where resistance is neglected and where resistance is compensated. Compensating the resistance utilizes the available power well as the blue curves lie only little below the green curves. Considering also the significantly more complex equations when taking the resistance into account, compensating for the resistance seems more feasible. Neglecting the resistance results in power and torque noticeably higher than what is achievable.
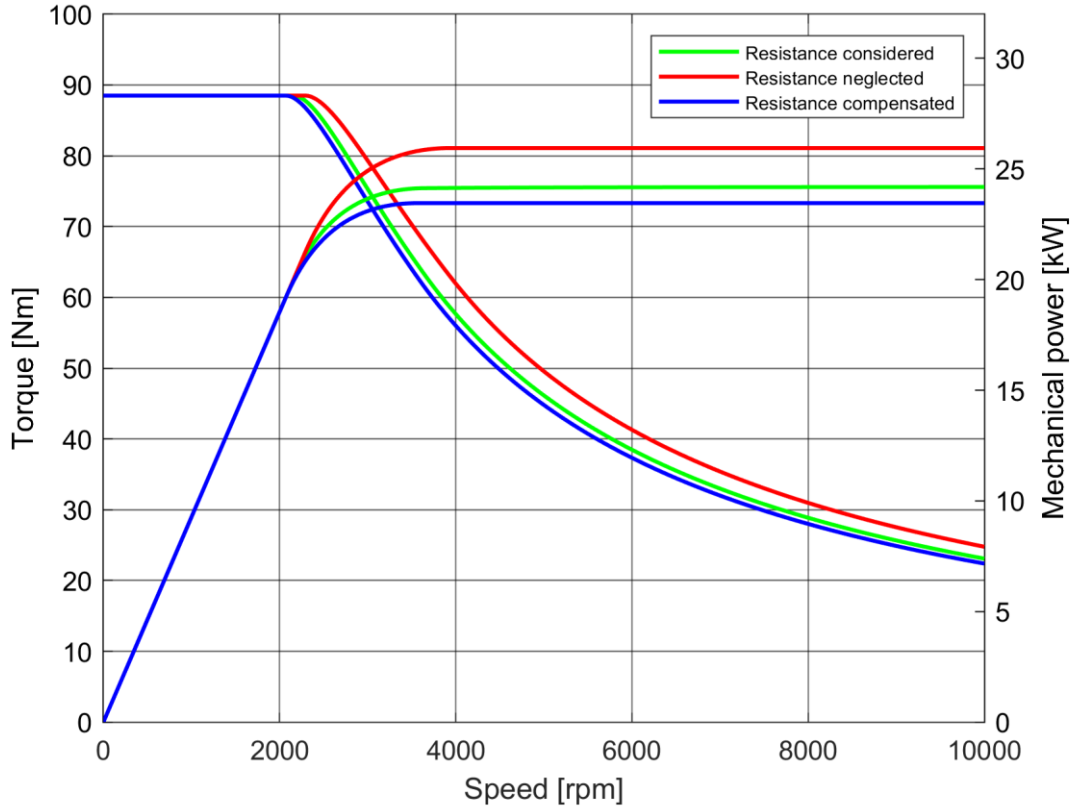
Figure 14. *Theoretical torque and power.*

In addition to the described flux weakening strategy there are other model based strategies as well. In [34, p. 84] it was stated that according to [26] and [35] constant voltage constant power (CVCP) control is widely used flux weakening method in the industry. However, [26] and [35] do not discuss CVCP control in their papers. Despite the unknown origin of this strategy, it is introduced here since it seems very applicable due to its simplicity. As the name implies, the strategy keeps constant voltage and constant power after the base speed is exceeded [34, p. 84]. At the base speed I_d is zero and steady state operation is assumed. If resistance is neglected, the q-axis voltage at the base speed is:

$$V_q = \omega_e\left(I_d L_d + \lambda_{pm}\right) = \omega_b \lambda_{pm}.$$
(2.38)

Since the voltage is kept constant, I_d for CVCP operation is obtained by solving Eq. (2.38) for I_d:

$$I_d = \frac{(\omega_b - \omega_e)\lambda_{pm}}{\omega_e L_d}.$$
(2.39)

As the power is kept constant, the product of the torque producing current I_q and speed must also remain constant:

$$I_q \omega_e = I_{qb} \omega_b. \tag{2.40}$$

At the end of the MTPA regime I_{qb} is equal to maximum phase current and for CVCP operation:

$$I_q = \frac{I_{ph,m} \omega_b}{\omega_e}. \tag{2.41}$$

Since $I_q \omega_e$ is constant, also voltage V_d is constant. The base speed can be solved using Eq. (2.34). Including the maximum resistive voltage drop in base speed calculation keeps the CVCP trajectory inside the voltage limiting circle in steady state operation. Figure 15 presents the combined MTPA and CVCP trajectory and the limiting circles. At speed below the base speed MTPA control is used and after that Eq. (2.39) is used to control current I_d. Equation (2.41) may be used to limit current I_q controlled by an outer control loop.
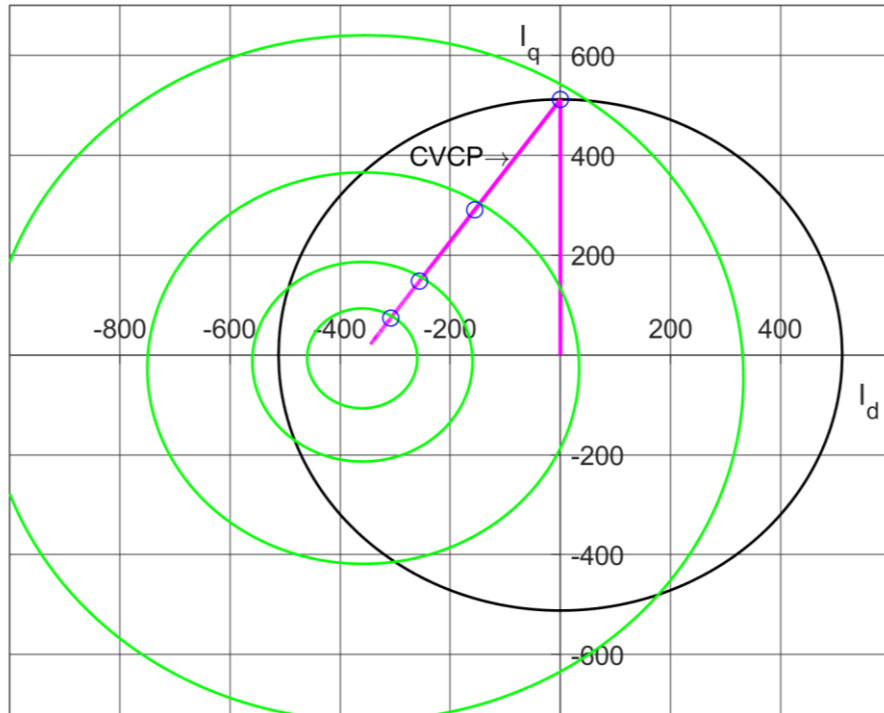
Figure 15. *CVCP trajectory and limiting circles (resistance considered).*

The blue markers correspond to the speeds of the voltage limiting circles. The markers are inside the circles because the resistance is compensated in the base speed calculation. Figure 16 presents the torque and power obtained by using CVCP trajectory. The power and torque of optimal flux weakening are presented in the same figure for comparison. The performance achieved with CVCP is significantly lower, but on the other hand the method is much simpler.
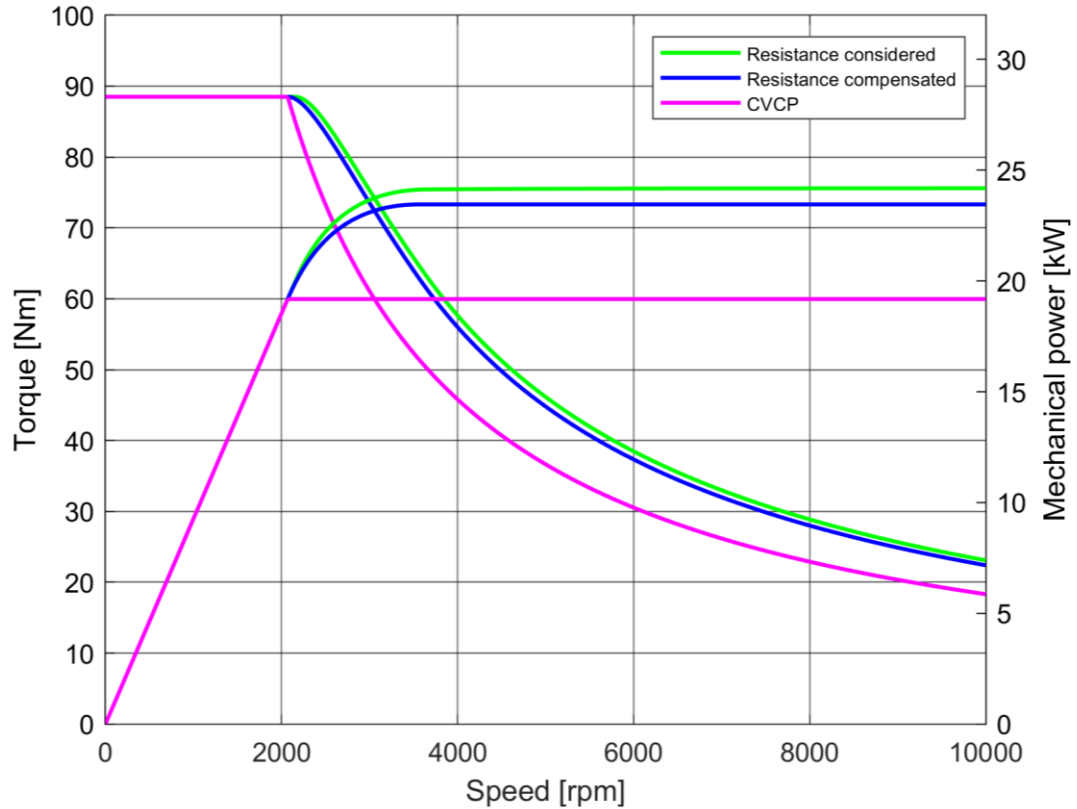
Figure 16.   *CVCP torque and power.*

The flux weakening analysis done here uses the maximum phase current instead of the rated current. For the SPM motor used in this analysis the rated phase current is four times lower than the maximum phase current. The motor can operate only short periods of time using maximum phase current without overheating. Inverters have similar limitations. This means that in many applications the motors mainly operates using currents much lower than the maximum current. In the application later introduced in this thesis the motor only operates near the rated current.

Another drawback of the CVCP method is that unnecessary I_d current is used when maximum available torque is not used. This is because the value of commanded I_q has

no effect on Eq. (2.39). This produces unnecessary resistive losses. When the requested torque is low, field weakening might be unnecessary. This is true until speed increases and the voltage limiting circle intersects the origin. After the base speed MTPA control could be used if it satisfies the voltage limitation. However, switching between MTPA and CVCP modes at speed beyond the base speed would result in step changes in current I_d. In addition, if the maximum current of the application is known and it is significantly below the motors maximum current, this known current could be used to calculate the base speed. This would essentially increase the base speed and avoid using unnecessary I_d. In applications where wider current range is used, the flux weakening method presented earlier would use current I_d more efficiently than the CVCP control.

2.4.3 Motor feedback

In the previous section it was shown that the motor controller uses rotor position information for several purposes. The measured phase currents are transferred to dq-frame using the measured electrical rotor angle. Similarly, the output of the current controller is transformed to form sinusoidal reference voltages for the inverter. In addition, if feedforward terms are used in the current controller, the rotor position information affects both the feedback dq-currents and the measured motor speed used to calculate the feedforward voltages. Outer control loops may also use the rotor position sensor to obtain speed feedback avoiding the use of multiple sensors. Typically motors use encoders, resolvers or hall sensors [6, p. 336]. High resolution optical encoders and resolvers provide good quality position and speed information for motor control and motion control but can impact the overall cost of the system significantly [36]. In addition these devices are delicate and require additional machine construction for mounting [37]. BLDC motors on the other hand only require three hall sensors as they don't use sinusoidal commutation [6, p. 335].

Despite the raw hall sensor position information being too coarse for control in dq-frame the study of using them started decades ago [38]. With three hall sensors distributed 120 electrical degrees apart a position resolution of 60 electrical degrees is obtained. A simple and popular approach to gain better position information using hall sensors is linear interpolation. By integrating the average velocity determined from hall sensor transitions a position estimation is obtained. [36] The speed is calculated using:

$$\omega_{e,est(i)} = \frac{\frac{\pi}{3}}{\Delta t_{(i-1)}}, \tag{2.42}$$

where $\omega_{e,est(i)}$ is the estimated speed for a hall period and $\Delta t_{(i-1)}$ is the elapsed time between the hall transitions for the period [39]. The rotor electrical angle is calculated using:

$$\theta_{e,est(k)} = \theta_{e,est(k-1)} + \omega_{e(i)}\big(t_k - t_{(k-1)}\big), \tag{2.43}$$

where $\theta_{e,est(k)}$ is the estimated electrical angle and $t_k - t_{(k-1)}$ is the sample period of the angle calculation.

Manufacturing tolerances cause offsets in hall sensor and rotor magnet placements making the transition angles different from ideal [40]. These unideal transitions make the measured estimated speed very noisy and have effect both on the rotor position estimation and speed used by outer control loops [36]. The placement of a sensor doesn't affect the time between edges from that given sensor. Therefore, calculating the time between edges of the same sensor instead of calculating the time between edges in general could improve the quality of speed estimation. However, if the hall signals are asymmetric this would still lead to errors in speed calculation. [39] Figure 17 presents hall sensor data measured from the SPM motor of which parameters were used in the flux weakening analysis. The motor was spun 100 rpm with an external torque source. The figure also presents the calculated state based on the hall signals and the sample count between the state transitions.
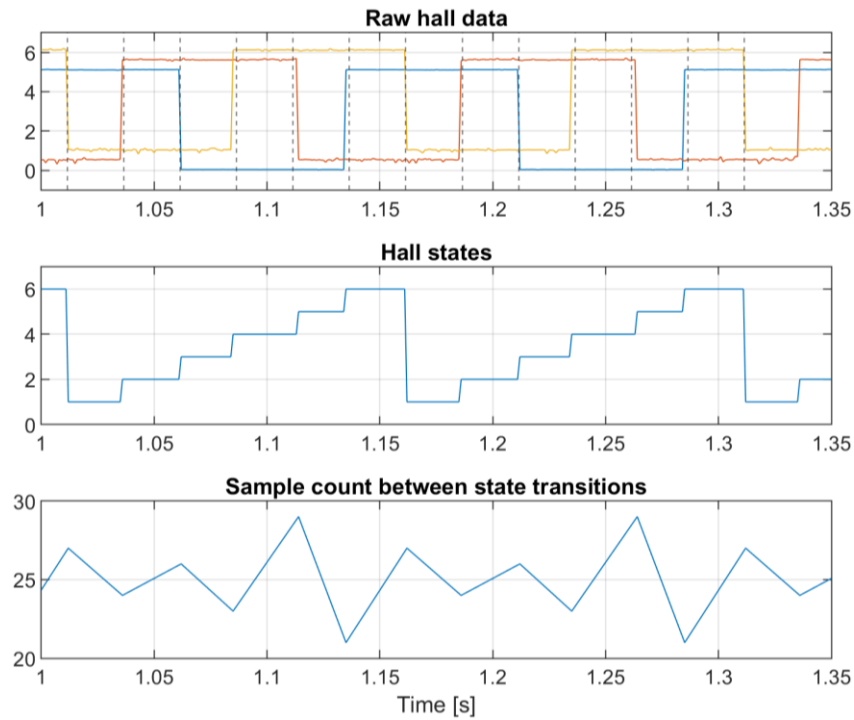

Figure 17. *SPM motor hall signals.*

Two of the hall signals are presented with small offset to make the data clearer. In addition, vertical dashed lines are presented at the locations where the transitions should ideally occur. The first vertical line is aligned with the falling edge of the yellow hall signal. The falling edges of the blue hall signal align with the dashed lines while the orange hall signal has slight offset. The offset is about 1 degree of mechanical angle. It can also be noted that all the hall signals are asymmetric staying high longer period than they stay low. The signals are high about 52 % of the period and low about 48 % of the period. The sample count between the transitions varies significantly due to the imperfections in the signals. This means that there is also significant noise in the estimated speed. The error in estimated speed leads to error in the estimated position and eventually to an incorrect motor control voltage [41]. According to [40] if vibration and noise are not of concern and the goal is only to produce commanded average torque these errors can be accepted. In [40] and [41] the actual transition angles were determined and used in the motor controller instead of the ideal angles. In both studies significant improvement was seen.

The position interpolation algorithm assumes that the speed stays constant between hall sensor signal transitions. This assumption fails at very slow speeds. In addition, in very slow speeds the counter that counts samples between hall state changes may experience overflow. Another hardware limitation is the frequency of the counter. As the motor speed increases the speed resolution decreases. [37] At powerup, at very slow speeds and after rotation direction changes the speed estimate cannot be calculated. A complete hall sector must be travelled to obtain an estimate for the speed. Square-wave commutation may be used at direction changes and at low speeds when the velocity estimate is not available [38]. The same equations can be used to calculate square-wave commutation reference currents that are used for sinusoidal commutation. Instead of the interpolated rotor angle the current hall sector is used to obtain rotor angle. Since the resolution of the hall sensors is 60 degrees electrical, this is also the largest possible error in position when using square wave commutation. If the rotor position is assumed to be in the middle of the hall sector the maximum error is 30 electrical degrees. Figure 18 presents the effect of this error. The assumed electrical angle is 0 degrees, commanded I_d is 0 A and commanded I_q is 100 A. If the angle error is 30 degrees, the actual I_q is about 87 % of the commanded value. For SPM motors the error in torque would be equal. Current I_d experiences much larger deviation. The error in current control along with poor quality speed information in very low speed makes the hall sensors undesirable for applications which require very high positioning accuracy.
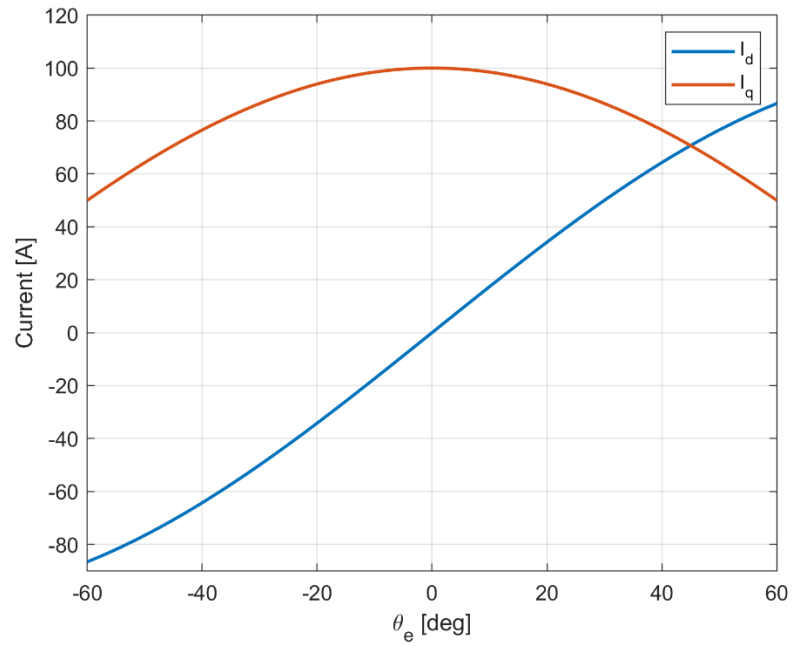
Figure 18. *DQ-currents as function of electrical angle.*

Sensorless rotor position sensing methods also exist. The motor BEMF can be used to estimate the rotor position, but this strategy fails at low speed due to low signal to noise ratio. Furthermore, rotor saliency can be used to estimate the rotor position. [42] Sensorless methods are not discussed in this thesis since industrial motion control systems usually employ position sensors.

3. MECHANICAL MODEL OF THE EMLA

In motion control system mechanical resonance is caused by compliance in the transmission. This compliance is usually between the motor and the load but can also be within the load if the load consists of multiple compliantly connected masses. Mechanical resonance is a fundamental problem in motion control.[6, p. 341] A block diagram of a two-mass model is presented in figure 19.
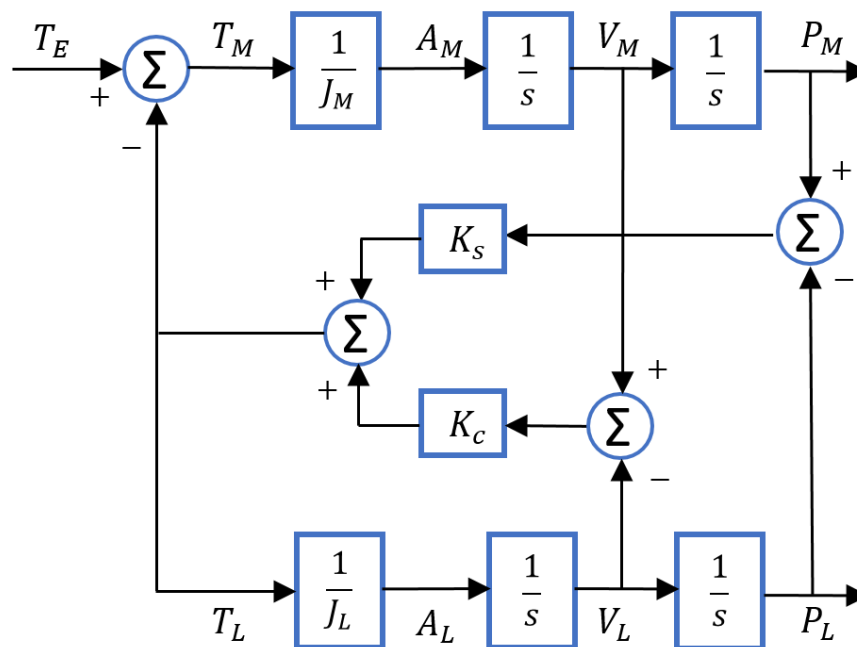
Figure 19. *Resonant load. Adopted from [6, p. 342].*

The electromagnetic torque T_E and the load torque T_L accelerate motor's rotating mass (J_M). The acceleration of the motor is integrated once to obtain velocity (V_M) and once more to obtain position (P_M) of the motor. Similarly, the load torque accelerates the load (J_L). The difference in motor and load positions cause compliance force which is proportional to stiffness K_S. A cross-coupled damping force is caused by difference in motor and load velocities and is proportional to damping coefficient K_C. Figure 19 is not displaying the terms that are usually referred to as friction. For example, a viscous friction term proportional to motor velocity could be added. The viscous friction usually has little

effect on mechanical resonance. The two-mass model has two natural frequencies. The first lower frequency called the antiresonant frequency is calculated using:

$$F_{AR} = \sqrt{\frac{K_s}{J_L}}.$$

(3.1)

The motor is difficult to move at this frequency as the energy transfers efficiently to the load. The motor may be almost still while the load oscillates at this frequency. This is also the frequency that the load would oscillate at if the motor was locked. The second higher natural frequency of the system called the resonant frequency is calculated using:

$$F_R = \sqrt{\frac{K_s(J_L + J_M)}{J_L J_M}}.$$

(3.2)

The motor is easy to move at the resonant frequency as both the motor and the load oscillate. Stability issues often occur at the resonant frequency or frequencies above that. [6, pp. 342–346]

Figure 20 presents the main components of the actuator. The actuator consists of multiple separate parts each having their own inertia, stiffness and friction properties.
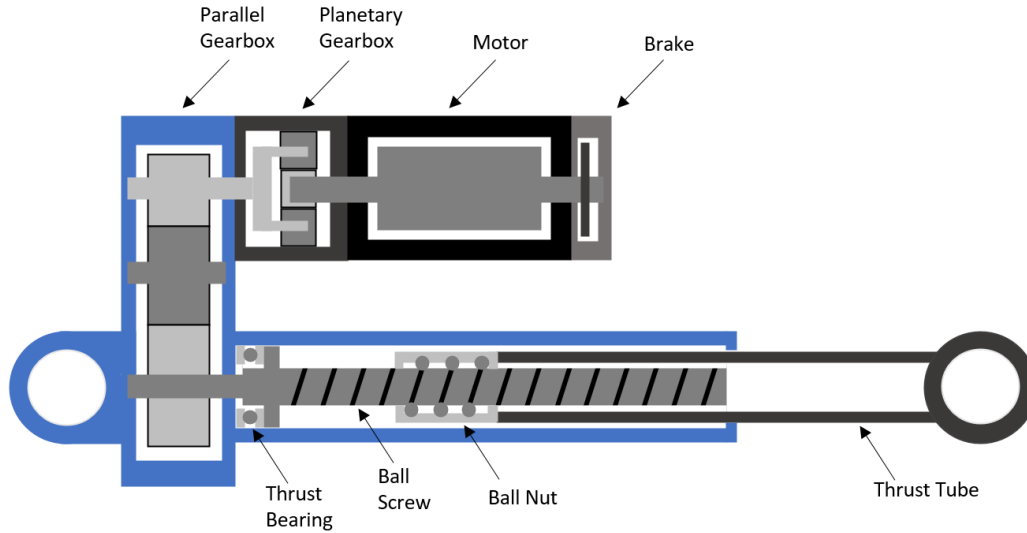

Figure 20. *Actuator's main components.*

In [43] a 2 degrees of freedom (DOF) and a 7-DOF model of ball screw drive system were compared with experimental results. It was found out that the 2-DOF model is sufficient unless the goal is to inspect the effect of individual components on the system. A

2-DOF model of the actuator and the load will be constructed in this thesis. In the following sections the parameters for the model will be derived. Table 3 presents the key parameters of the EMLA studied in this thesis.

Table 3.   EMLA parameters.

Maximum Static Force	550 kN
Maximum Dynamic Force	280 kN
Maximum speed	44 mm/s
Stroke	640 mm
Ball screw size	63x16 mm
Gear ratio	24,35

These parameters along with CAD files provided by the EMLA manufacturer will be used to derive parameters for the mechanical model.

3.1   Inertia of the EMLA

Figure 21 presents the inertia components of the actuator. As the inertia of the planetary gearbox is given at the input shaft by the manufacturer, J_1 is used to combine inertia of the motor and the planetary gearbox. J_2 and J_3 are the inertias of the first two gears in the parallel gearbox. J_4 combines the inertia of the third gear in the planetary gearbox and the inertia of the ball screw. m_1 is the mass of the thrust tube and ball nut.
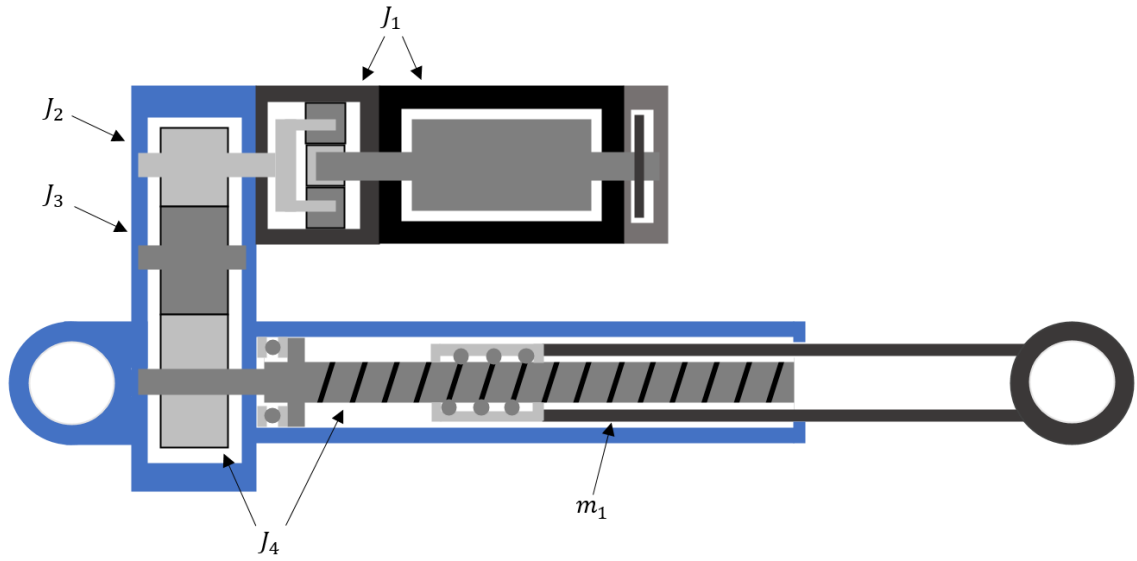
Figure 21. *Inertia of the actuator.*

To form the two-mass model of the system the inertia of the actuator must be expressed at a single point. The equivalent inertia of the whole actuator J_{eq} is calculated by expressing the kinetic energy of the actuator as function of motor speed:

$$\frac{1}{2}J_{eq}\omega_m{}^2 = \frac{1}{2}J_1\omega_m{}^2 + \frac{1}{2}J_2\omega_2{}^2 + \frac{1}{2}J_3\omega_3{}^2 + \frac{1}{2}J_4\omega_4{}^2 + \frac{1}{2}m_1 v^2. \tag{3.3}$$

When the speeds of the components are expressed with respect to the motor speed one obtains:

$$J_{eq}\omega_m^2 = J_1\omega_m^2 + J_2\left(\frac{\omega_m}{n_{plg}}\right)^2 + J_3\left(\frac{\omega_m}{n_{plg}n_{g1,2}}\right)^2 + J_4\left(\frac{\omega_m}{n_{tot}}\right)^2 + m_1\left(\frac{\omega_m P}{n_{tot}2\pi}\right)^2, \tag{3.4}$$

where n_{plg} is the gear ratio of the planetary gearbox, $n_{g1,2}$ is the gear ratio of the first gear pair in the parallel gearbox, n_{tot} is the total gear ratio and P is the lead of the screw. Equation (3.5) is obtained by simplifying Eq. (3.4) as:

$$J_{eq} = J_1 + \frac{J_2}{n_{plg}{}^2} + \frac{J_3}{\left(n_{plg}n_{g1,2}\right)^2} + \frac{J_4}{n_{tot}{}^2} + m_1\left(\frac{P}{n_{tot}2\pi}\right)^2. \tag{3.5}$$

The equivalent inertia may as well be expressed as a mass connected to the thrust tube by setting the kinetic energies at both ends of the actuator equal and by solving for m_{eq}:

$$\frac{1}{2}m_{\text{eq}}v^2 = \frac{1}{2}J_{eq}\omega_m^2, \tag{3.6}$$

$$m_{\text{eq}}v^2 = J_{eq}\left(\frac{n_{\text{tot}}2\pi v}{P}\right)^2, \tag{3.7}$$

$$m_{\text{eq}} = J_{eq}\left(\frac{n_{\text{tot}}2\pi}{P}\right)^2. \tag{3.8}$$

The equivalent mass or inertia of a component is obtained by dividing the mass or inertia with the square of mechanical reduction. Using this information, the masses or inertias may be expressed with respect to any component in the system. The equivalent mass of the load (boom) is obtained similarly using the mechanical reduction. The relationship between actuator and joint velocity is:

$$\omega_j = \frac{v}{r}, \tag{3.9}$$

where ω_j is joint angular velocity, v is actuator linear velocity and r is the moment arm. The moment arm depends on the joint position. The equivalent mass is then obtained by expressing the kinetic energy of the load:

$$E_L = \frac{1}{2}J_b\omega_j^2, \tag{3.10}$$

$$E_L = \frac{1}{2}\frac{J_b}{r^2}v^2, \tag{3.11}$$

$$m_L = \frac{J_b}{r^2}, \tag{3.12}$$

where E_L is kinetic energy of the load, J_b is inertia of the boom about the joint axis and m_L is equivalent mass of the load. Table 4 presents the equivalent masses of the load and the components of the actuator.

Table 4.   Equivalent masses of the system.

Component	Equivalent Mass [kg]
Load	101 770
Motor	203 960
Planetary Gearbox	10 330
Parallel Gear 1	259.0
Parallel Gear 2	1141
Parallel Gear 3	3628
Ball screw	1042
Ball Nut	10.0
Thrust Tube	30.0

It is noted that the load and the motor dominate the inertia of the system. The inertia of the motor and the planetary gearbox consist 97.2 % of the actuator's total inertia. The ball nut and the thrust tube have practically no impact on the total inertia.

3.2   Stiffness of the EMLA

Similarly to the inertia also the stiffness of the actuator must be expressed using a single value. Figure 22 presents the components considered. $k_{\tau 1}$ consists of torsional stiffnesses of the motor's shaft and planetary gearbox. $k_{\tau 2}$ consists of torsional stiffness of the coupling between the gearboxes and the stiffness of parallel gearbox's first gear contact. $k_{\tau 3}$ is the torsional stiffness of the second gear contact in the planetary gearbox. $k_{\tau 4}$ is the torsional stiffness of the screw shaft and k_1 is the combined linear stiffness of the thrust bearing, ball screw, ball nut and thrust tube.
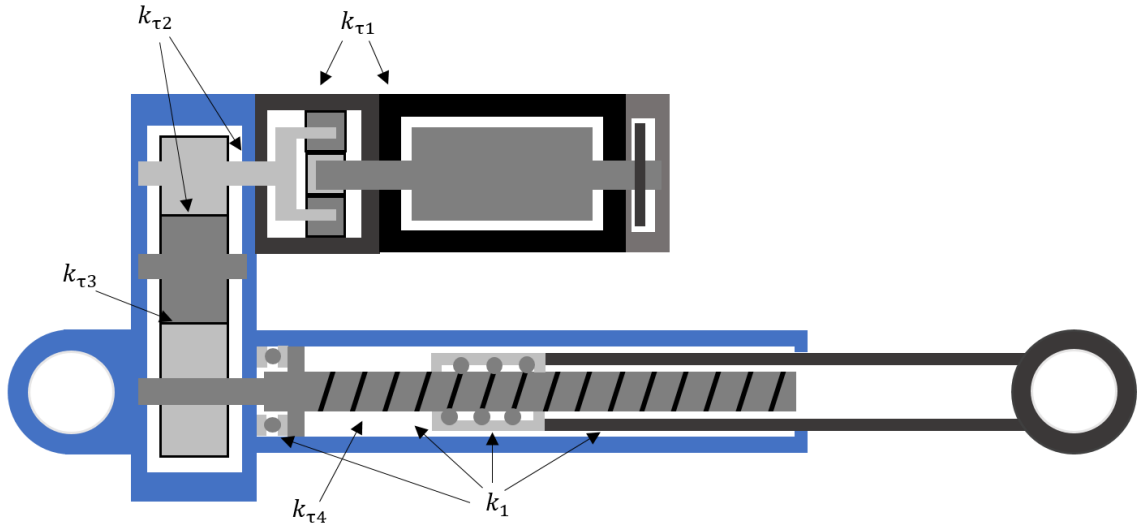
Figure 22. *Stiffness components of the actuator.*

To express the equivalent stiffness at the motor shaft the elastic potential energy of the actuators is expressed as function of motor shaft twist. Note that for clarity θ is used instead of $\Delta\theta$ and x is used instead of Δx.

$$\frac{1}{2}k_{\tau eq}\theta_m{}^2 = \frac{1}{2}k_{\tau 1}\theta_1{}^2 + \frac{1}{2}k_{\tau 2}\theta_2{}^2 + \frac{1}{2}k_{\tau 3}\theta_3{}^2 + \frac{1}{2}k_{\tau 4}\theta_4{}^2 + \frac{1}{2}k_1 x_1{}^2 \tag{3.13}$$

By substituting $x = F/k$ and $\theta = T/k_\tau$, we obtain:

$$k_{\tau eq}\frac{T_m{}^2}{k_{\tau eq}{}^2} = k_1\frac{T_m{}^2}{k_{\tau 1}{}^2} + k_2\frac{T_2{}^2}{k_{\tau 2}{}^2} + k_3\frac{T_3{}^2}{k\tau_3{}^2} + k_4\frac{T_4{}^2}{k_{\tau 4}{}^2} + k_1\frac{F^2}{k_1{}^2}. \tag{3.14}$$

By expressing the torques and forces as function of motor torque Eq. (3.15) is obtained:

$$\frac{T_m{}^2}{k_{\tau eq}} = \frac{T_m{}^2}{k_{\tau 1}} + \frac{\left(T_m n_{plg}\right)^2}{k_{\tau 2}} + \frac{\left(T_m n_{plg} n_{g1,2}\right)^2}{k_{\tau 3}} + \frac{\left(T_m n_{tot}\right)^2}{k_{\tau 4}} + \frac{\left(\frac{T_m n_{tot} 2\pi}{P}\right)^2}{k_1}. \tag{3.15}$$

Finally, Eq. (3.16) is obtained by simplifying Eq. (3.15). It may be seen that Eq. (3.16) is the expression of stiffness of springs connected in series with each term multiplied by the square of mechanical reduction.

$$k_{\tau eq} = \left(\frac{1}{k_{\tau 1}} + \frac{n_{plg}{}^2}{k_{\tau 2}} + \frac{\left(n_{plg} n_{g1,2} \right)^2}{k_{\tau 3}} + \frac{n_{tot}{}^2}{k_{\tau 4}} + \frac{\left(\frac{n_{tot} 2\pi}{P} \right)^2}{k_1} \right)^{-1} \tag{3.16}$$

The stiffness can also be expressed as equivalent linear stiffness at the thrust tube. This is done by setting the elastic potential energy at both ends of the actuator equal. Solving k_{eq} is done similarly as solving for $k_{\tau eq}$ above:

$$\frac{1}{2} k_{eq} x^2 = \frac{1}{2} k_{\tau eq} \theta_m{}^2, \tag{3.17}$$

$$\frac{F^2}{k_{eq}} = \frac{F^2 \left(\frac{P}{n_{tot} 2\pi} \right)^2}{k_{\tau eq}}, \tag{3.18}$$

$$k_{eq} = k_{\tau eq} \left(\frac{n_{tot} 2\pi}{P} \right)^2. \tag{3.19}$$

Some of the stiffnesses in Fig. 22 involve several components. The combined stiffnesses of the components are calculated by using the formula of springs connected in series. For example, k_1 is calculated by:

$$k_1 = \left(\frac{1}{k_{bearing}} + \frac{1}{k_{screw}} + \frac{1}{k_{nut}} + \frac{1}{k_{tube}} \right)^{-1}. \tag{3.20}$$

The stiffnesses of some components are given by the manufacturers and some must be calculated. For linear springs such as the thrust tube the stiffness is calculated using:

$$k = \frac{EA}{L} \tag{3.21}$$

, where E is young's modulus of the material, A is area of the cross-section and L is the length of the object [44, p. 506]. For torsional springs such as the motor shaft the stiffness is calculated using:

$$k_\tau = \frac{GJ_p}{L}, \tag{3.22}$$

where G is shear modulus of the material, J_p is the polar second moment of area and L is the length of the object [44, p. 505]. For cylindrical cross-sections the polar second moment of area is calculated using:

$$J_p = \frac{\pi D^4}{32},$$

(3.23)

where *D* is the diameter of the cylinder [44, p. 236]. Table 5 presents the equivalent linear stiffnesses of the actuator components at the thrust tube. The stiffnesses are sorted from the least stiff to the stiffest. Since the length of the screw under load depends on the actuator position also the stiffness is function of actuator position. Stiffnesses of the ball screw are expressed as range from actuator minimum length to actuator maximum length.

Table 5. Equivalent stiffnesses of actuator components.

Component	Equivalent Stiffness [N/µm]
Screw (compression)	752 - 3960
Thrust tube	1060
Ball Nut	2000
Thrust Bearing	2000
Gear contact 1	19 300
Screw (torsion)	22 400 - 118 000
Gear contact 2	22 600
Gear 1 coupling	320 000
Motor shaft	1 260 000
Planetary gearbox	5 660 000

Figure 23 presents the stiffness of the actuator with different combinations of components considered. Starting from the left the two least stiff components are included. Progressing to the right more components are included. The stiffnesses are calculated at three different actuator positions: fully retracted, mid-stroke and fully extended.
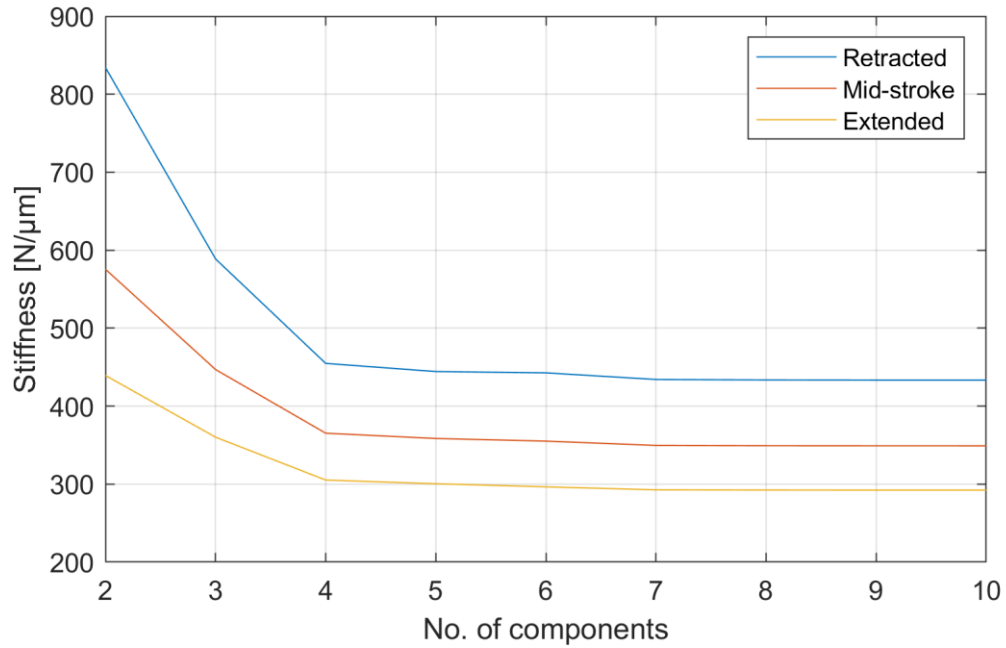
Figure 23. *The effect of ignoring components.*

It is seen that relatively good estimation of the stiffness may be obtained by including only the four least stiff components. The effect of the components from the motor to screw torsion is small. At mid-stroke excluding all but the four least stiff components result in error of 4.4 %.

Now that the inertia and stiffness are both known the natural frequencies of the system may be calculated using Eqs. (3.1) and (3.2). As the stiffness of the actuator is function of actuator position so are the natural frequencies. Figure 24 presents the antiresonance frequency and resonance frequency of the two-mass model. It may be seen that the frequencies are higher at shorter actuator positions as the stiffness of the actuator is higher.
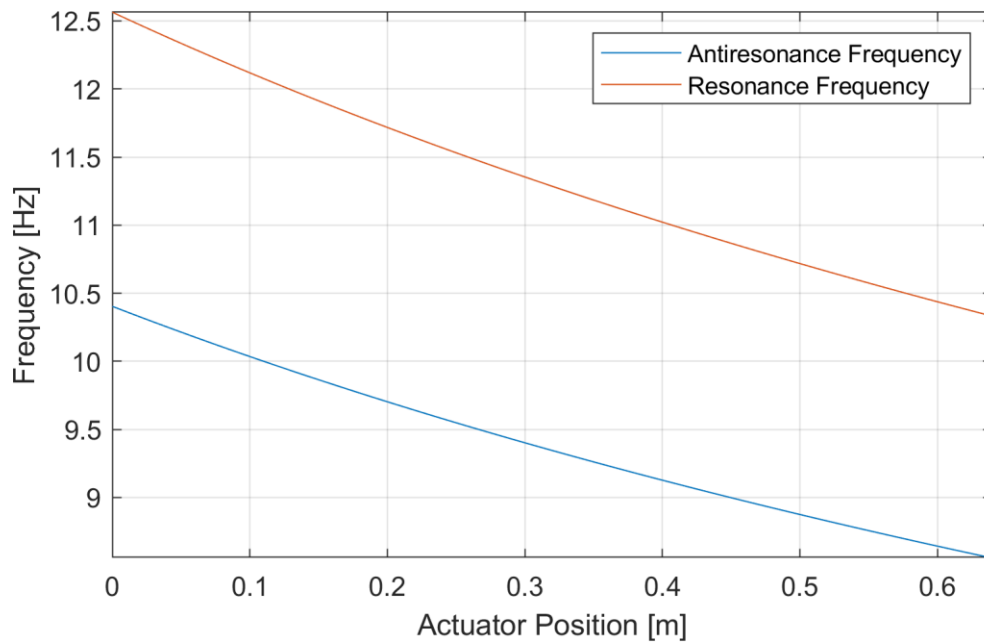
Figure 24. *Natural frequencies of the system.*

It may be seen that the frequencies are higher at shorter actuator positions as the stiffness of the actuator is higher. In many applications the mechanical leverage that the actuator has on the load changes with actuator position. This also affects the natural frequencies as it changes the equivalent load inertia. This is not considered here.

3.3   Friction of the EMLA

Several components in the actuator involve friction and cause losses in the actuator. Multiple papers have studied the friction of ball screw drives. Different types of ball nuts exist, and this makes comparing the results of different papers difficult. Figure 25 presents three types of ball nuts and their preload methods. Preload is used to eliminate backlash and to increase stiffness [45]. When using a single nut, the preload may be obtained by using oversized balls or by introducing a skip in the lead of the nut. The double nut is preloaded by forcing the two nuts apart by inserting a spacer or a spring between the nuts. With skip lead and double nut constructions the balls have two contact points and only half of the balls carry the load. With the oversized balls construction, the balls have four contact points, and all the balls carry the load. The single nut with oversized balls is more compact but less efficient as skidding occurs in the non-loaded side of the ball [46].
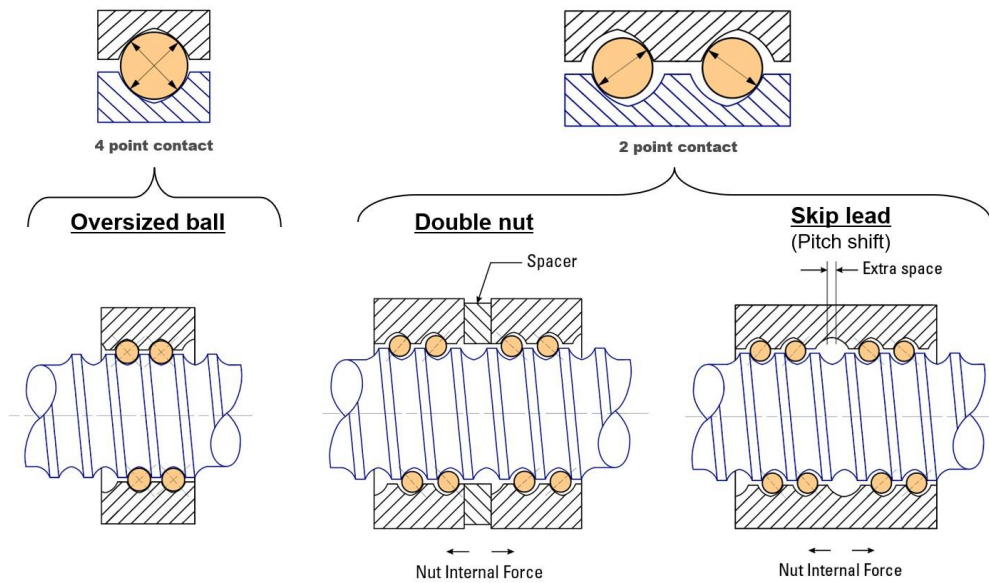
Figure 25. *Different types of ball nuts [46].*

As ball screws are widely used in feed drive systems the friction of the screw is also often studied in these conditions. However, the load of the screw in feed drive systems may be much smaller compared to EMLA. Some of the observations of feed drive systems may still be applicable to EMLAs. In [47] the power consumption of different components in a feed drive system was evaluated with different types of ball nuts. It was found out that the ball nut accounts for most of the mechanical losses and that the losses increase almost linearly with speed. This indicates that the viscous friction is very small. However, it was not discussed what kind of lubrication was used. In [48] an analytical model for ball screw was developed. The model predicted efficiencies of 90-92 %. In [49] this model was compared against experimental data and it was found out that the friction predicted by the model was too small. In [50] another analytical model was developed and compared with experimental data. The model exhibited similarities to experimental data, but the efficiency predicted by the model was higher. In [51] a model for ball screw friction was developed based on experimental results. The model predicts the friction coefficient at different speeds and loads but obviously experimental data is needed to obtain the parameters for the model.

All the models require lots of parameters that cannot be found in manufacturers' catalogs and the accuracy of many of the models seems to be very low. The efficiency of other transmission components such as gearboxes and bearings also affect the total friction of the actuator. Manufacturers of these components provide little information about the

efficiency of these components. For example, for planetary gearboxes the efficiency is usually provided only in a single operation point. The efficiency of planetary gearboxes is often reported to be over 95 %. As so little information is provided a simple assumption must be made to model the friction of the actuator. In this thesis a constant mechanical efficiency is assumed, and the value will be determined in the later sections from experimental data.

In a spring-mass system the cross-coupled damping is also a form of friction. Instead of being proportional to velocity of components with respect to frame it is proportional to velocity difference between the components. The cross-coupled damping increases system stability by dampening the oscillations but unfortunately steel provides only little dampening [52, p. 342]. In this thesis the damping is estimated to be one percent of the critical dampening of a 1-DOF spring-mass system. The damping coefficient is calculated using:

$$K_c = \frac{1}{100} \cdot 2\sqrt{K_{eq} m_{load}}, \tag{3.24}$$

where m_{load} is the equivalent mass of the load.

4. MOTOR TEST BENCH

A motor test bench was constructed to test the motor and motor controller that are intended to be used to power the EMLA. The test bench involves two motors that are connected by a HBM T40B torque transducer and necessary couplings. The motor that is to be used in the EMLA is referred to as *test motor* and the motor providing the load torque is referred to as *load motor*. The load motor is Omron 1S servo motor with 23-bit resolution encoder. It is powered by appropriate Omron 1S servo drive. Figure 26 presents CAD model of the motor test bench.
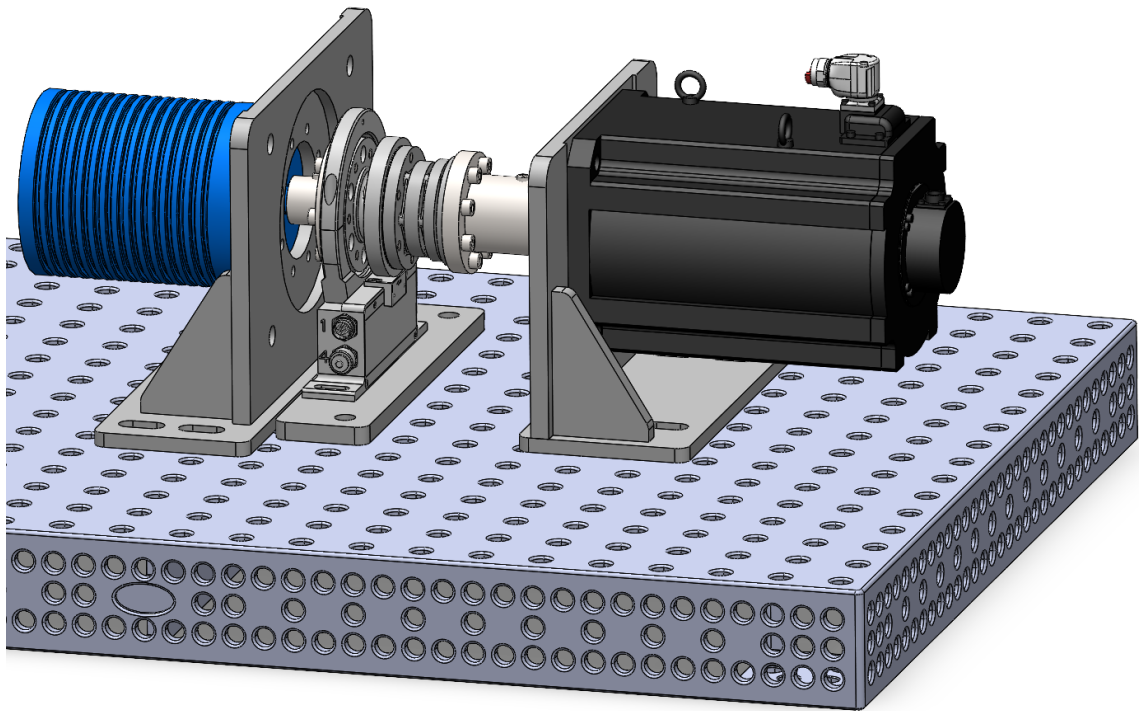
Figure 26.   *Motor test bench CAD model.*

Sevcon Gen4 controller used for the test motor is intended for vehicle applications and does not provide the necessary features to implement position control. Motion control is implemented using a dSpace controller that feeds torque reference to the load motor controller. The motor test bench provided the means to develop the control system safely. The motor test bench also made it possible to validate the simulation model of the motor and controller independently of the rest of the actuator. In the next section the

simulation model of the motor test bench is presented to illuminate both the simulation model and the structure of the real system.

4.1   Simulation model

Simulations are carried out in Matlab Simulink environment. Figure 27 presents the top-level of the motor test bench simulation model. The simulation model is divided into sub-systems that present the components of the real system with a few exceptions. The test motor's electromagnetic model and mechanical model are in separate subsystems. The load motor's model is in the same subsystem with the mechanical model.

The load motor is modeled as an ideal torque source as it is designed for applications requiring much higher accuracy and dynamics than the test motor. The load motor's task is to provide constant load torque and high-quality position and velocity feedback. The load motor and drive can perform these tasks well enough to justify the simplified mod-elling. The Load Motor FB subsystem only models the position and velocity feedback of the load motor. The load motor controller and dSpace controller communicate using EtherCAT. Feedback values are received at 1 ms intervals.
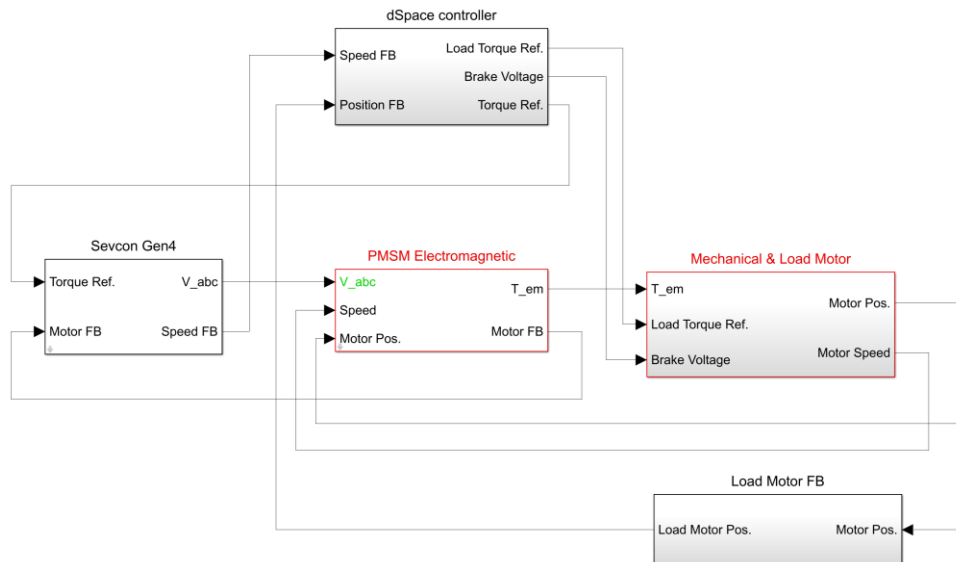

Figure 27.   *Motor test bench model's top-level.*

Figure 28 presents the proportional-integral-derivative (PID) controller inside the dSpace controller subsystem that controls the test motor. The position error is calculated using desired position provided by a higher-level controller and measured position provided by the load motor drive. The speed error is calculated using desired motor speed provided by a higher-level controller and measured speed provided by the load motor controller. CAN bus is used for communication between dSpace and test motor controller. The test motor controller limits the control loop frequency to 50 Hz.

In addition, a gravity compensation torque that is equal to load motor torque reference is added to the torque reference. The constant torque of the load motor mimics the load caused by gravity that the EMLA is subjected in the application of this thesis. The higher-level controller is also responsible of controlling electromechanical brake of the test motor. The brake is engaged when the motor is stationary. The Torque Off signal is used to reset the integrator when the brake is engaged and switch test motor torque off. The higher-level controller is not presented in detail in this thesis.
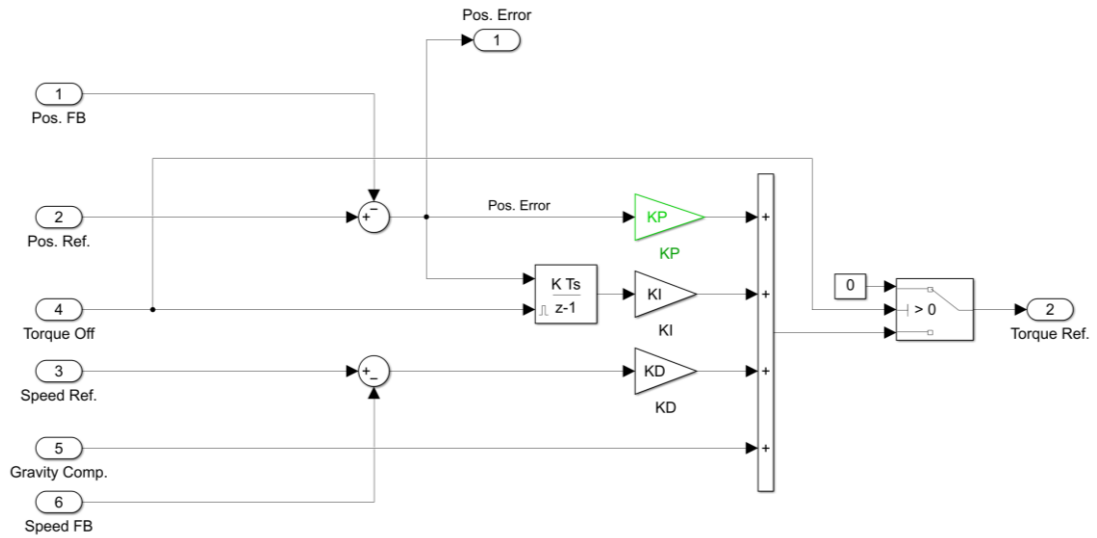
Figure 28.   *PID controller with gravity compensation.*

Figure 29 presents the Sevcon Gen4 controller model. MTPA and CVCP control are used in the flux controller. It is not known what kind of flux weakening algorithm is used in the controller, but CVCP was chosen for modeling due to its simplicity. The current control is modeled utilizing PI controllers with feedforward terms. Dynamic saturation is modeled to favor I_d and V_d. In the Hall Sensor Processing subsystem linear interpolation algorithm discussed in subsection 2.4.3 is implemented to obtain rotor position. The rotor position is used to calculate currents I_d and I_q from the measured phase currents. The motor speed is calculated by measuring elapsed time between hall transitions and is

then fed through a low pass filter. The Hall sensor signals and measured phase currents are obtained from the Motor FB signal. The estimated rotor position is also used to transform V_d and V_q voltages to phase voltages. The inverter is not modelled, and the requested phase voltages are assumed to follow ideal relations.
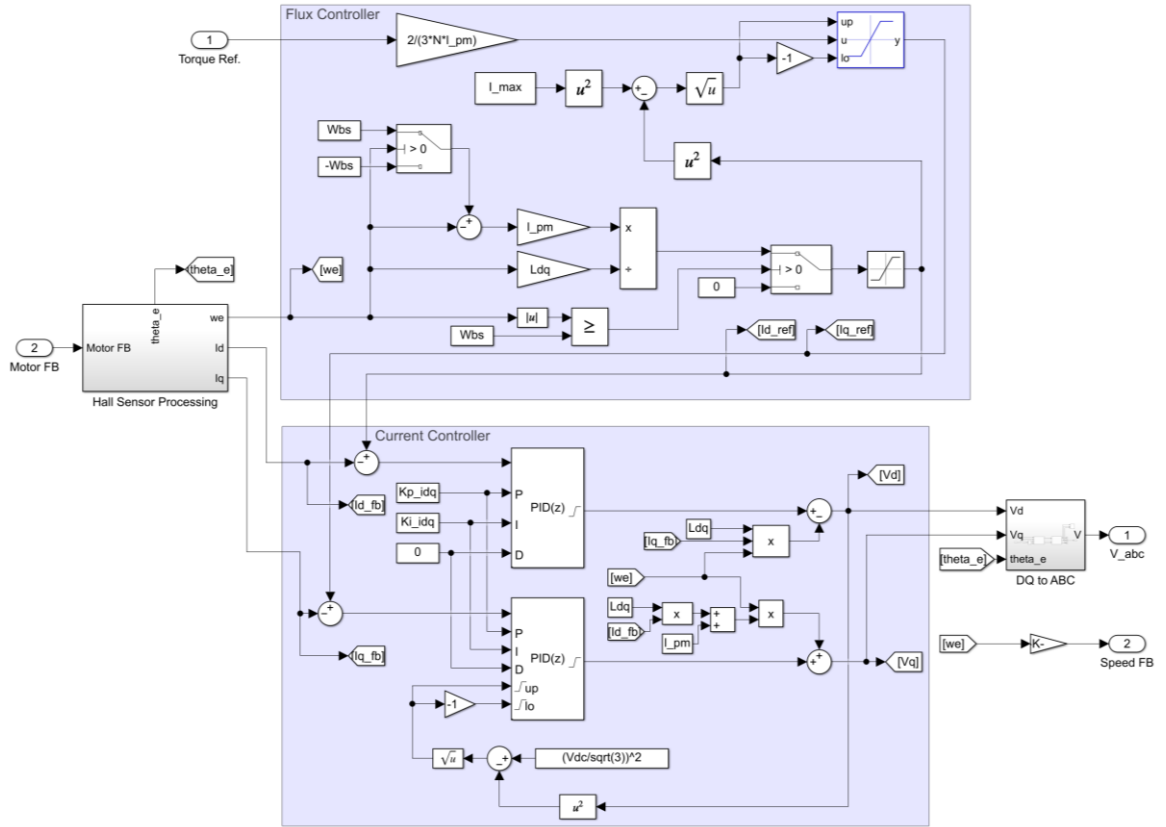
Figure 29.   *Sevcon Gen4 subsystem.*

Figure 30 presents the test motor's electromagnetic model. The model is implemented in dq-frame and motor position provided by the mechanical subsystem is used to transform phase voltages to dq-voltages. Motor position is also used to transform the dq-currents to phase currents for feedback. It seems that opposite transformations are performed in the controller model and in the motor model. However, it is important to understand that in the controller the transformations are performed using estimated motor position provided by the hall sensor interpolation algorithm instead of the actual motor position. The PMSM Electromagnetic subsystem also includes model for the Hall sensors which outputs the hall signals based on the measured switching positions of the actual motor.
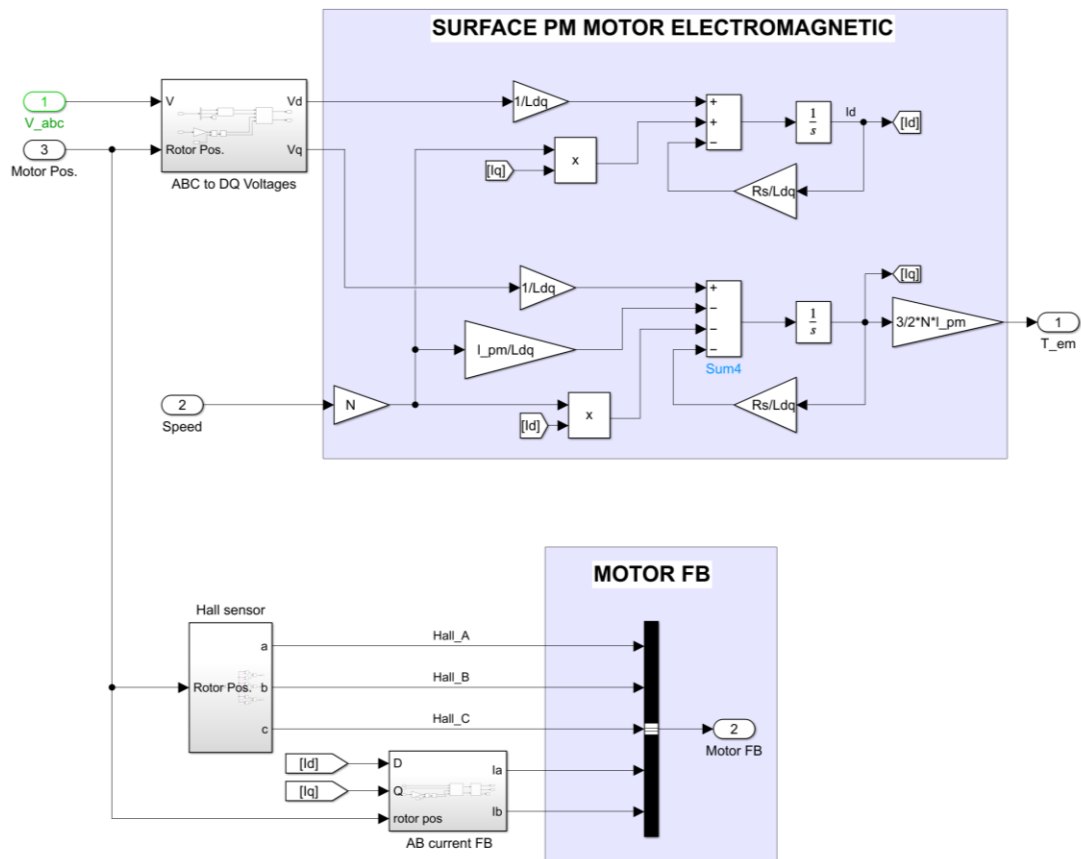
Figure 30.   *PMSM Electromagnetic subsystem.*

Figure 31 presents the motor test bench mechanical model and the load motor model. The mechanical model is a 2-DOF spring-mass model that also includes friction terms for both motors. The torque sensed by the torque transducer is the signal that is sum of spring compliance torque and damping torque. The parameters for the spring-mass model are easier to obtain than the parameters for the EMLA as there are no gear reductions. The stiffness is simply calculated using the equation for series connected springs and the inertias are sums of individual component's inertias. These parameters are not discussed here in detail.

Figure 31. *Mechanical & Load Motor subsystem*

The friction terms include viscous friction terms and static friction terms. The viscous friction is proportional to speed while the static friction's magnitude is constant. A signum function could be used 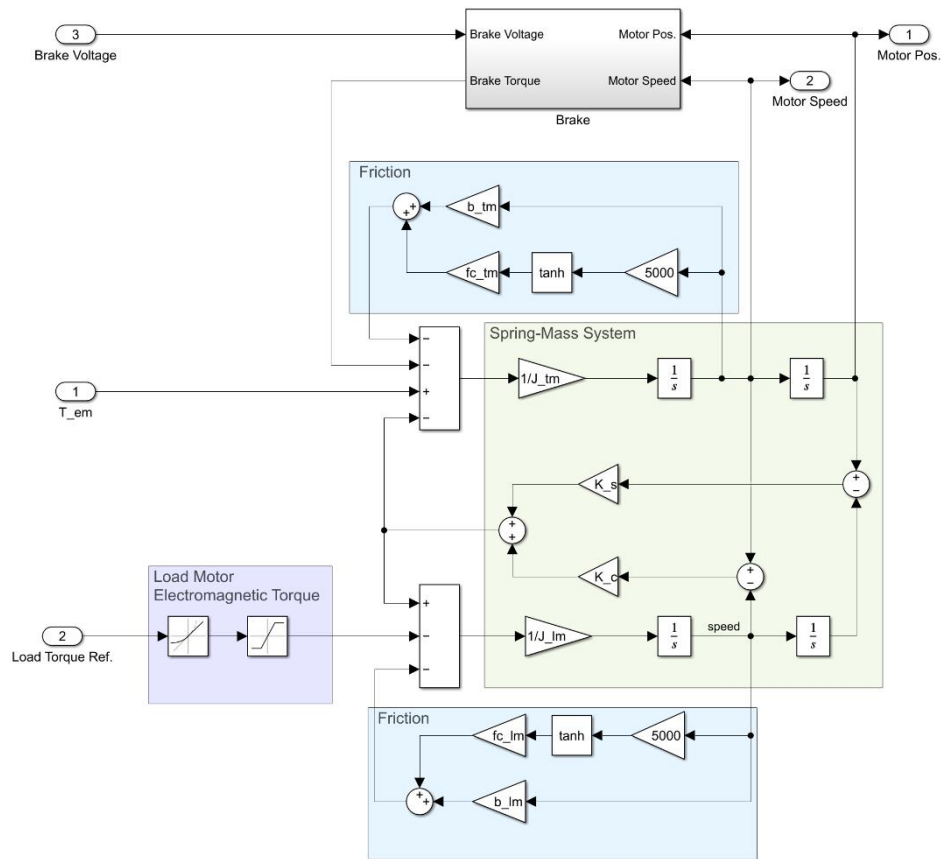to obtain value of 1 or -1 depending on the turning direction. This value could then be used to multiply the magnitude of the static friction. However, to avoid discontinuities hyperbolic tangent and a switching gain of 5000 is used instead. This provides continuous transition on narrow band between 1 and -1 as the turning direction changes.

Figure 32 presents measured values of the friction and linear regressions that give parameters for motor friction models. The motors were spun in both directions with different speed for several seconds and the average torque value was calculated. The torque transducer is not well suited for measuring torques this small and this might affect the results. Furthermore, due to hardware limitations analog output of the transducer is used instead of digital output. The analog signal contains some interference which deteriorates the measurement.

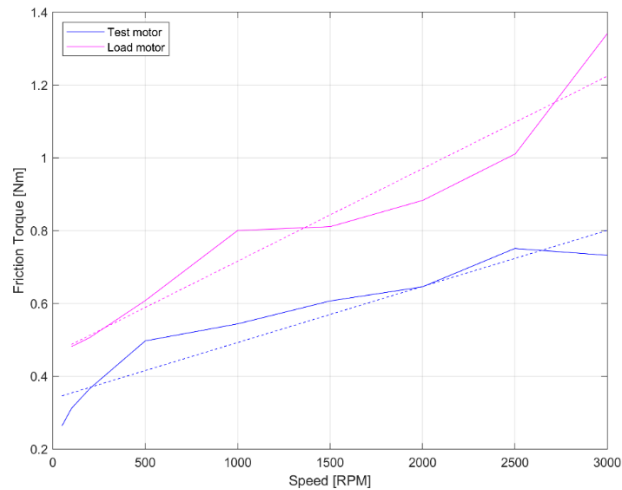***Figure 32.*** *Motor friction measurements.*

The mechanical subsystem includes a separate subsystem for the electromechanical brake of the motor. This subsystem is presented in figure 33. The brake subsystem is also a spring-mass system making the actuator mechanical model a 3-DOF system. However, when the brake is locked the system reduces to 2-DOF system.
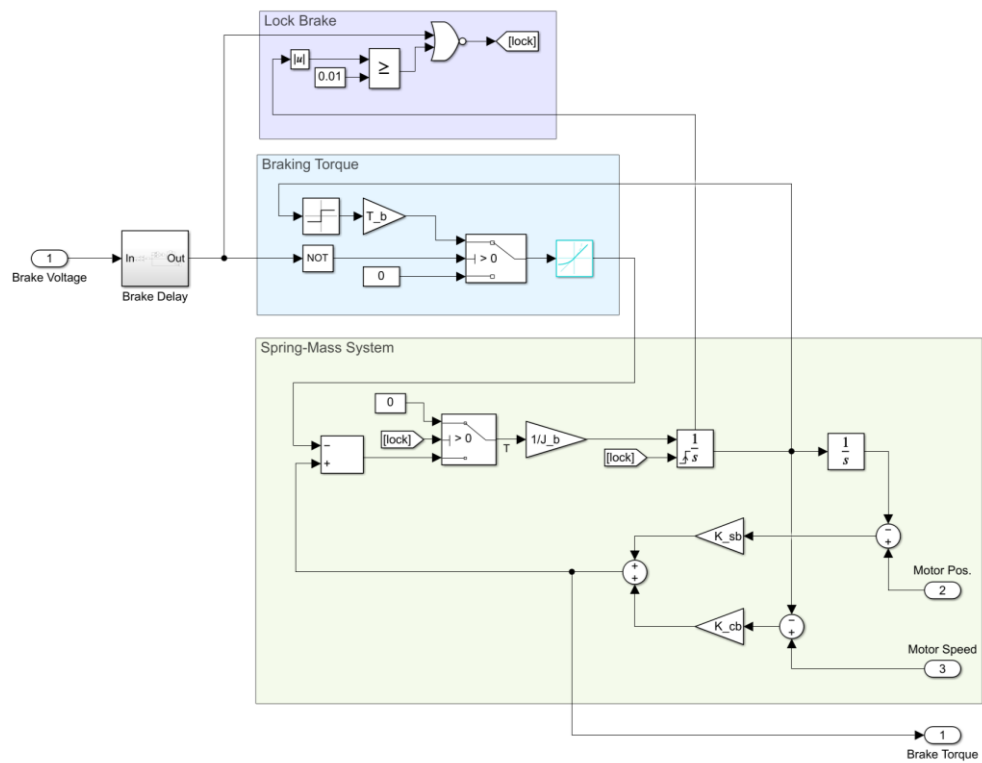
Figure 33. *Brake subsystem.*

The brake has little effect on the system despite adding some inertia. Modeling the compliance of the brake is still necessary as the brake may be engaged when the motor is not perfectly still. The brake is modelled to apply a constant braking torque when applied in move. The locking of the brake is modelled by resetting the speed integrator when speed falls below a set threshold.

4.2   Test results

A cubic polynomial trajectory was chosen for testing to obtain similar motion as in the boom. Figure 34 presents the response of both the simulation model and real system. The first graph displays the position reference, position feedback and position error. The dashed lines with right-hand side y-axis presents the position error. The second graph displays the reference speed and feedback from the test motor controller. The third graph displays the reference speed and feedback from the load motor controller.
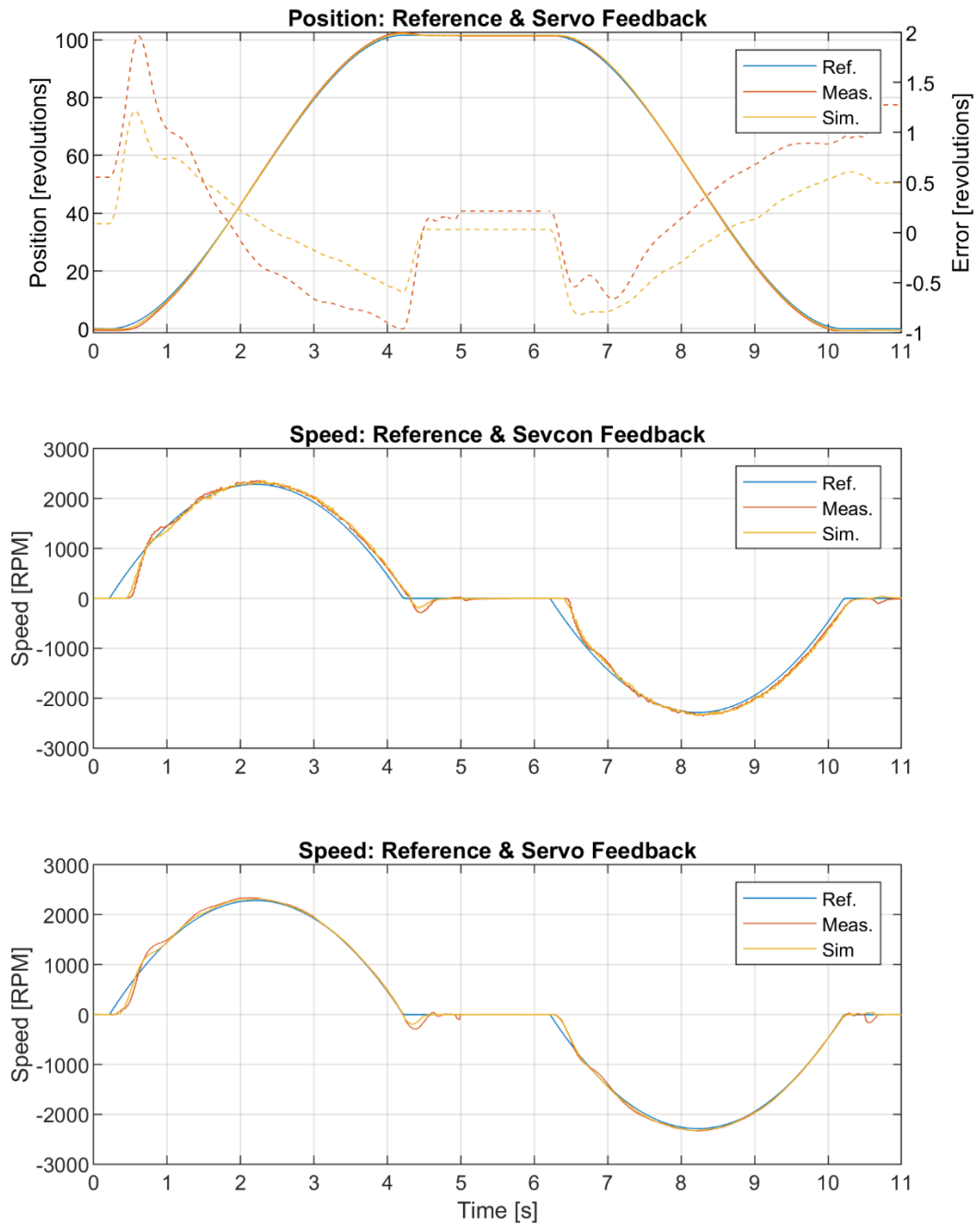
Figure 34. *Position and velocity tracking.*

The simulation model corresponds well with the real system. Both position and velocity tracking are very similar. The performance of the system is good although the velocity shows some oscillation. The test motor's speed feedback shows a noticeable delay when compared to feedback of the load motor. This delay is easily noticed especially when accelerating from rest. This delay causes instability and limits the magnitude of controller gains that can be used.

Figure 35 presents feedback currents and measured torque. The I_q current of the simulator agrees well with the measurement data. The slightly lower magnitude is to be expected as only resistive and friction losses of the motor are modelled. I_d current shows much larger difference especially when the motor speed is at its highest. It seems that the test motor controller does not apply flux weakening even though the base speed of the motor is exceeded. This implies that the controller does not use CVCP but some more advanced flux weakening algorithm. I_d current shows more ripple than I_q in both results. This is because I_d current changes much more rapidly with phase angle. The hall sensor interpolation algorithm and misalignment of the sensors causes some ripple in the estimated rotor position, and this shows most noticeably in I_d current. The peaks are much more frequent but the 20 ms interval in the CAN bus communication filters most of them out.

The averages of the torque values are also very close but the magnitude of the ripple is higher in the real system. However, it is not known how much of the ripple is caused by interference in the analog signal and how much is actual torque ripple. Some torque ripple is to be expected due to hall sensor interpolation algorithm and misalignment of the sensors. In addition, motor design affects the torque ripple and this is not considered in the simulation model. Large spike in torque occurs in data of real system at 5 s and in simulation data before 11 s. These are result of brake closing while the motor is spinning. The delay in the speed feedback is problematic when the motor is tried to hold still for closing the brake. The motor stays still only for a short period before braking into move again. There is also delay in the closing and opening of the brake. Obviously, Hall sensors are not well suited for accurate positioning.
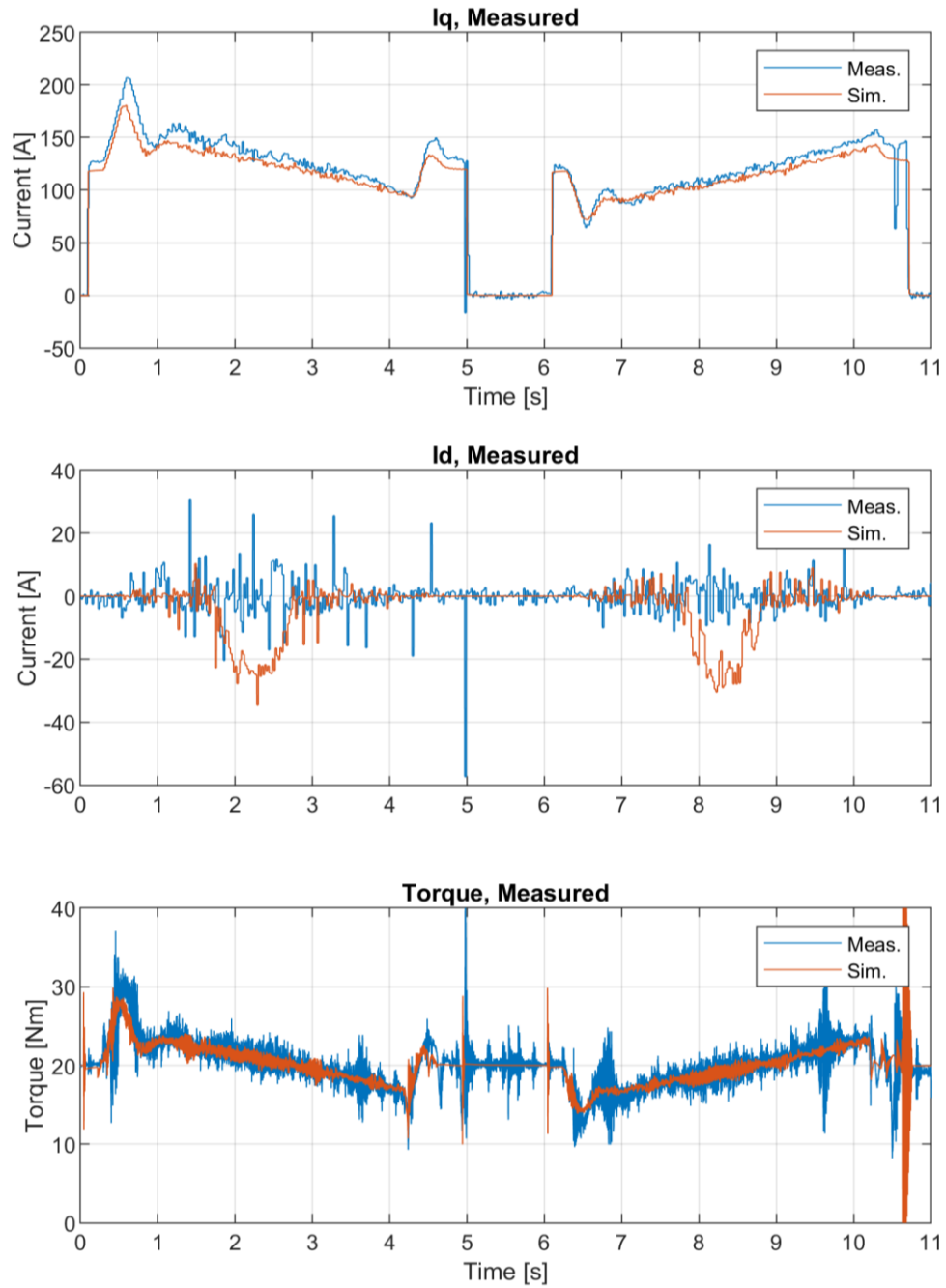
Figure 35. *Measured currents and torque.*

The motor test simulation model agrees well with the test results. Especially the factors related to controllability seem to be modelled in sufficient detail. The flux weakening algorithm and torque ripple are not of great importance in the tests that are carried out with the boom.

5. BOOM WITH EMLA

The boom is similar to system presented in figure 1. The boom has multiple joints and actuators but only one joint (lift joint) is considered in this thesis. The rest of the boom is assumed rigid making the boom a 1-DOF application. The simulation model of the boom is constructed, and the simulation results will be compared with measuring data of the real system. Instead of the test motor being connected to another motor it is connected to the EMLA in the boom. Although the mechanics of the system are very different there is much in common with the two systems. Same motor and motor controller are used, and the dSpace controller is also very similar. Some parts of the motor test bench simulation model can be used without any modification.

5.1 Simulation model

Figure 36 presents the top-level of the boom simulation model. The top level includes the boom's mechanical model that is implemented using Simscape Multibody. Simscape Multibody forms and solves the equations of motion for the rigid bodies in the system. Mass parameters of the bodies are obtained from a CAD model. The boom's support and the boom are connected by a joint which senses the joint angle. In the real system there is a joint angle sensor that communicates with dSpace controller using CAN bus. This sensor loop is running at 100 Hz.

The dSpace controller subsystem is very similar to the motor test bench's controller. Similar cubic trajectory is constructed that is then fed into a PID controller. The main difference is that the PID controller controls actuator position instead of motor position. The controller calculates the actuator position from the joint angle. The gravity compensation feedforward term is calculated using joint angle and mass parameters of the bodies.

Figure 36. *Top-level view of the boom simulation model.*

Figure 37 presents the EMLA subsystem. This subsystem contains the interface between the Simscape Multibody model and the actuator's mechanical model. The Simscape Multibody model contains a translational joint that takes actuator force as input and outputs the position and velocity of the actuator. The position and velocity are used in the spring-mass model of the actuator inside the EMLA Mechanic subsystem.

The electromagnetic model of the motor is modelled using the same subsystem as in motor test bench model. This block provides the electromagnetic torque used in the mechanical model.
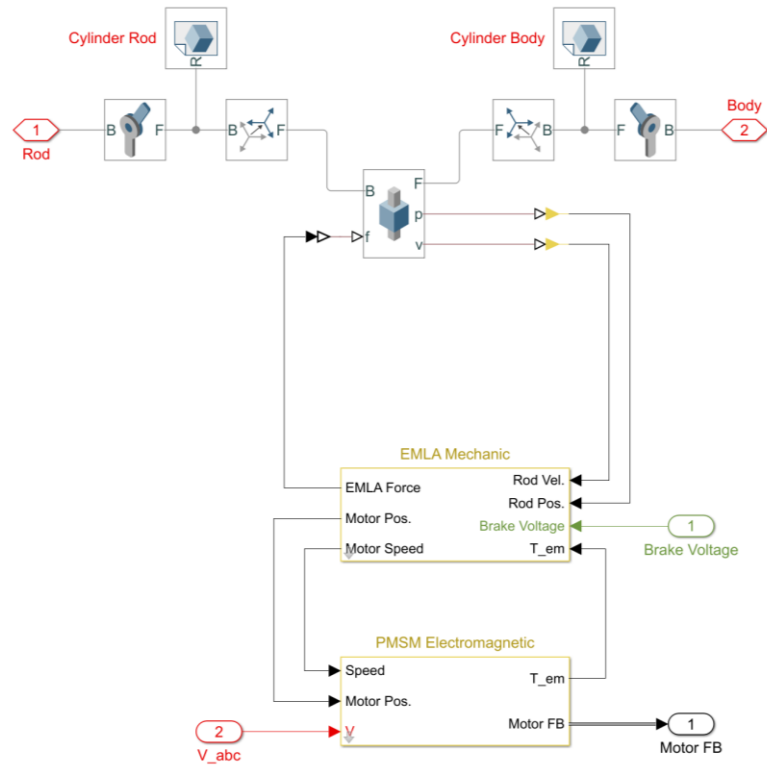
Figure 37. *EMLA subsystem.*

Figure 38 presents the mechanical model of the actuator. The subsystem includes spring-mass model of the actuator and the Brake subsystem. The stiffness of the actuator is calculated as function of actuator position using equations presented in chapter 3. The damping coefficient and inertia are also calculated using equations presented in that chapter. The friction force is modelled to fulfill assumption of constant efficiency using

$$F_f = \frac{F_{act}}{\eta} - F_{act},$$

(5.1)

where F_{act} is actuator force and η is efficiency of the actuator not including motor friction losses. The motor friction is modelled similarly as in the motor test bench model. The gearbox reduction and screw lead are used to transform between the motor speed and EMLA linear speed. Similarly, torque at the motor shaft is obtained from the actuator force using the transmission reduction.
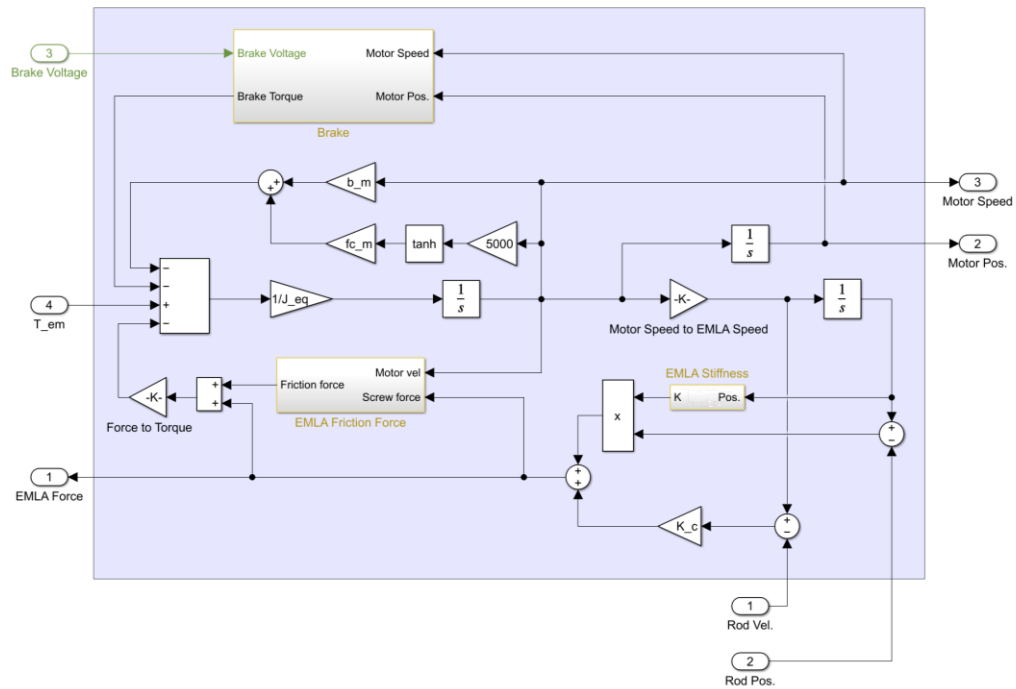
Figure 38. *EMLA Mechanic subsystem.*

To obtain a value for the actuator efficiency used in the friction model measuring data was analyzed. The motor test bench was used to form a table of values that link the actual torque to requested torque at different speeds and loads. This way the actual torque at motor shaft is known well at different load conditions. To calculate the efficiency of the actuator the measured motor torque is compared with the torque that would be needed if there were no losses at all. The torque required without losses may be analytically solved using the mass parameters of the bodies. The accuracy of the efficiency calculation depends on the accuracy of the mass parameters. To evaluate accuracy of the mass parameters average torque during the motion is compared with the analytical solution. A trajectory was driven repeatedly with the boom to obtain average torque at different joint angles. The average values of torques in up and down motions were then calculated. Figure 39 presents the averages of motor shaft torques in up and down directions. In addition, averages of up and down values and analytical values are presented. The analytical solution only takes static load caused by gravity into account. The torque required for acceleration should not be present in the measured average value (yellow plot) since the trajectory is symmetric. The accelerations torques should cancel each other out in opposite motion directions. This also applies to friction.
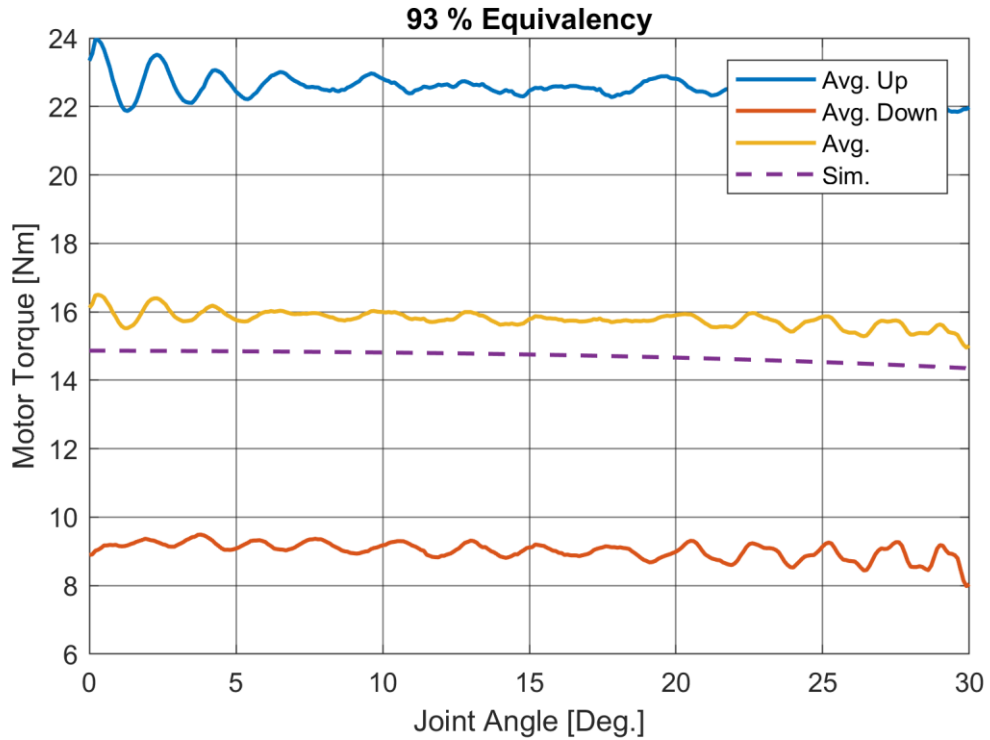
Figure 39. *Motor torque as function of joint angle.*

It was found out that the torque of the analytical solution is approximately 93 % of the measured value. The offset between the analytical solution and measured average value is relatively constant throughout the motion. The offset may be a result of mass parameter inaccuracy. It is also possible that the magnitude of friction is not equal in both motion directions. However, the accuracy is sufficient to evaluate efficiency for the friction model.

Figure 40 presents the mechanical and electrical energy as function of joint angle. The electrical energy is calculated by measuring battery voltage and current flowing between battery and the motor controller. Both total and mechanical efficiencies are lower in the downward motion. Based on the efficiency of the upward motion efficiency of 66 % is used for the friction model.
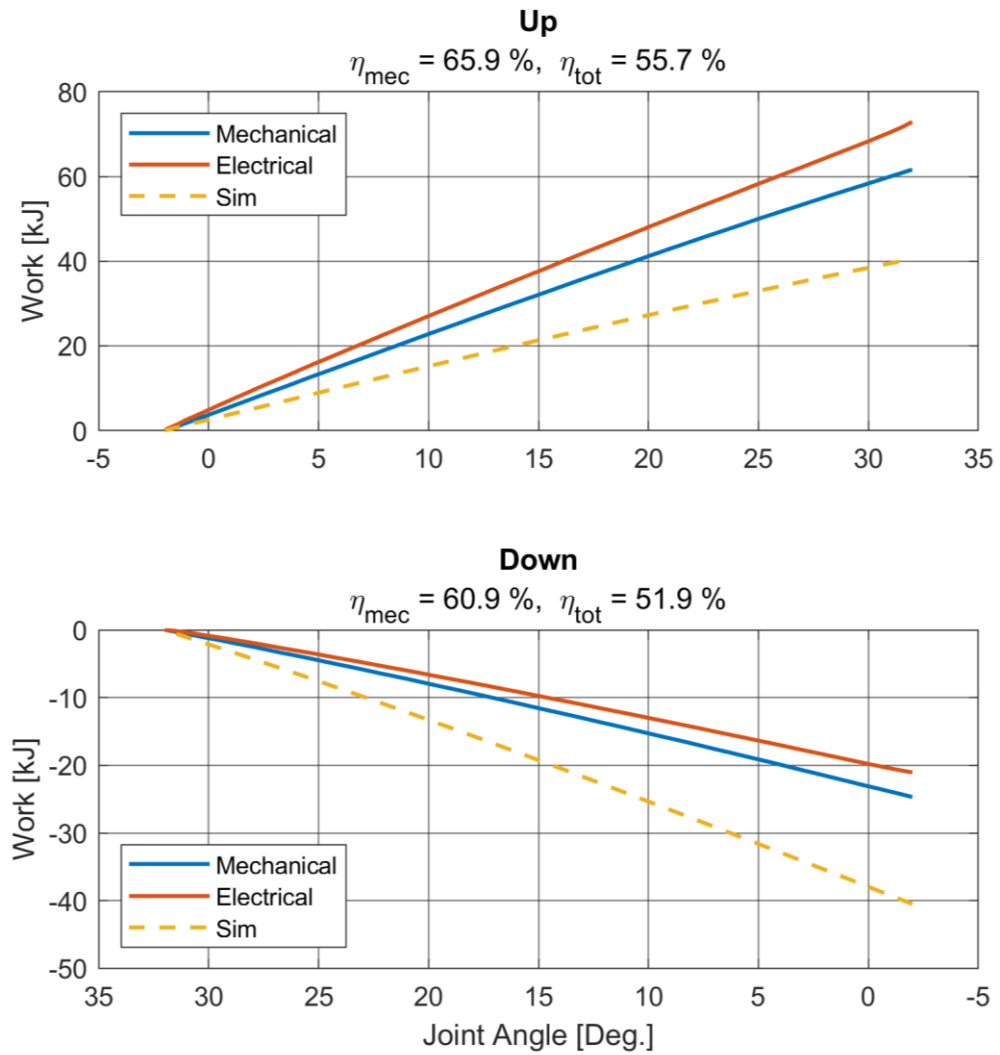
Figure 40. *Mechanical and electrical energy.*

The efficiency calculations may be inaccurate due to error in mass parameters and due to low accuracy of battery current measurements. In addition, the effect of joint friction is unknown. The values presented in this thesis should not be used to draw conclusions about EMLA efficiency in general. However at least in this case, the mechanical efficiencies of 65.9 % (up) and 60.9 % (down) were much lower than initially expected.

5.2   Test results

Figure 41 presents the simulation results and measurement data of the boom. The measurement data shows larger error in position tracking than the simulation data. The velocity tracking is more similar as both show similar oscillation throughout the motion. In addition, both show large lag and following overshoot in the beginning of the motion. The I_q current of the measurement data is larger in the first part of the trajectory but more similar in the second part of the trajectory. This might be due to inaccuracy of the friction model or due to inaccuracy of the mass parameters. The current of the measurement data does not drop to zero as the motor brake does not close. The controller does not engage the brake if the position error is above set limit.
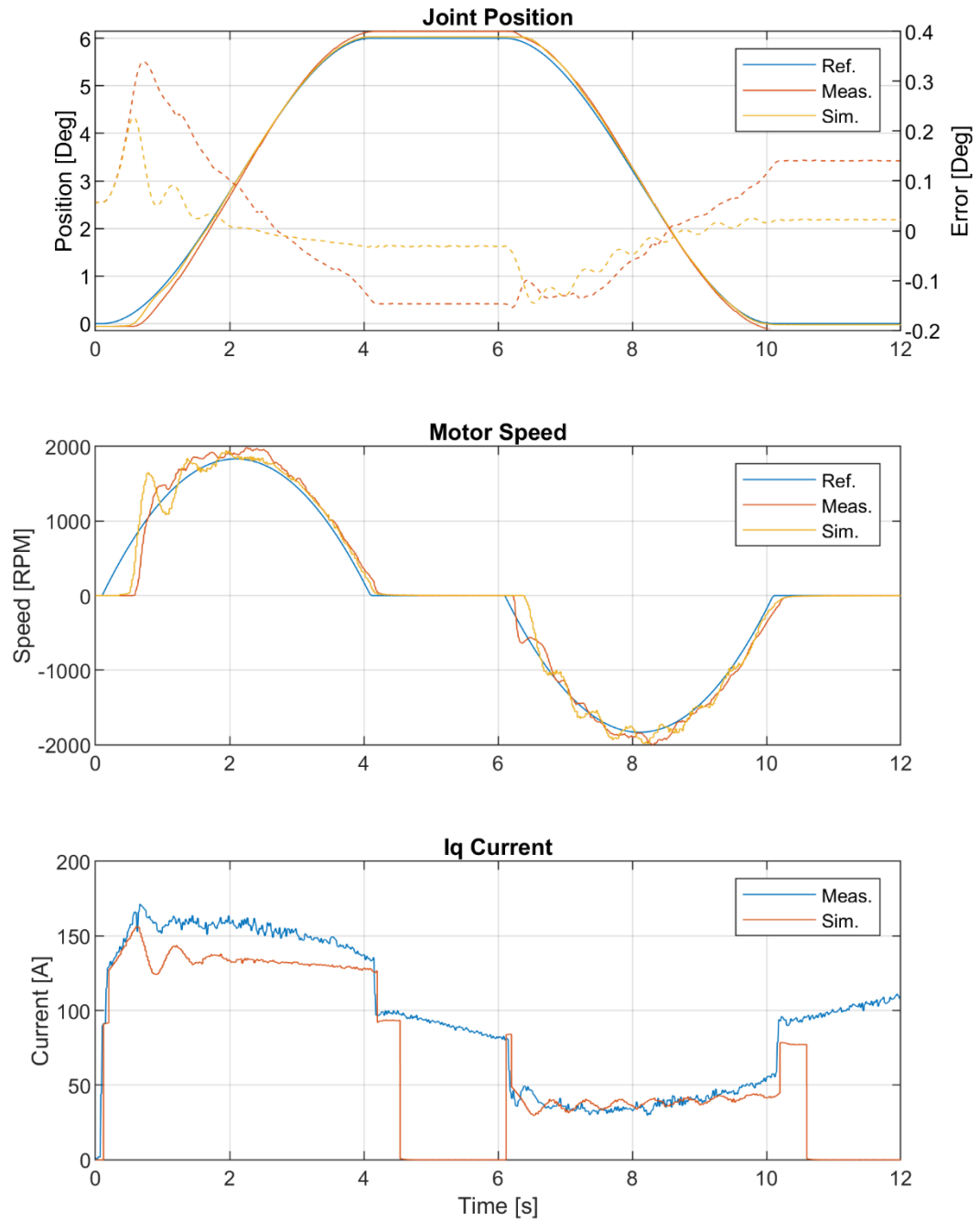
Figure 41. *Measurement and simulation result of the boom.*

The differences in positioning performance might be due to the inaccuracy of the friction model. The friction of the actuator involves some stiction that makes the positioning more difficult. Larger torque is required to get actuator in the move when stiction is present. The real system manages to close the brake eventually, but it takes longer time and is not visible in the graph. While the simulation model fails to present the problems in positioning it certainly presents the oscillation in speed. The oscillation was found out to be a persistent problem and it could not be solved with controller parameter tuning. The simulation model assumes that the boom is rigid, but it in fact is quite flexible and distinct

deflection is present. Oscillations in speed and initial jerk when accelerating from stand still tend to awaken oscillations in the flexible structure. To move the boom smoothly better tracking of the speed reference is required.

To determine if the oscillation in speed is due to structure elasticity or due to poor control performance some additional simulations were carried out. The control loop frequency was increased from 50 Hz to 1000 Hz. The 10 ms sampling interval of the position sensor was not changed. In addition, hall sensor feedback was replaced with ideal feedback. The goal was to simulate a system where current motor and motor controller were replaced by a servo system using high quality motor sensor and higher loop frequency. The controller remained unchanged but derivative gain was multiplied by 10. The faster control loop allowed to increase this gain significantly without stability issues. Figure 42 presents the simulation results.
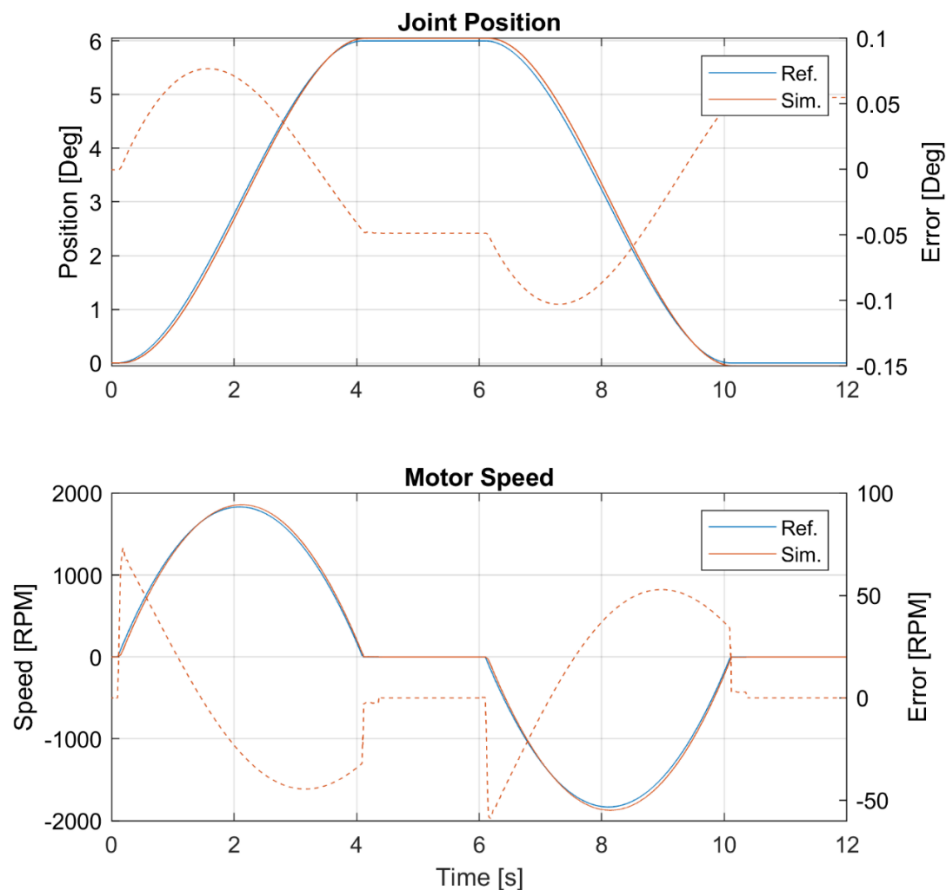

Figure 42. *Simulation results with improved speed feedback.*

The oscillations in speed are completely gone and both position and speed tracking are significantly better. By tuning the controller more even better response could be obtained but the changes were kept little intentionally. The results indicate that the problems in

the current system are largely caused by low control loop frequency and large delays. According to simulations by replacing the current motor and controller with a conventional servo drive system the controllability should increase significantly. Clearly using CAN Bus and low-resolution motor sensor to implement the control loop of the motor in this application result in poor performance. CAN Bus should allow higher loop frequency, but the 50 Hz limit is set by the hardware that was used in this project. Using Hall sensor as the feedback device in motion control applications seems undesirable as there are much better alternatives available.

6. CONCLUSIONS

In this thesis a simulation model for a 1-DOF boom actuated by an EMLA was developed. First necessary theory and mathematical equations related to the system were presented. The structure, operating principle and common control methods of PMSM were introduced. Spring-mass mass model of the actuator was developed and equations for obtaining the parameters used in the model were presented.

To validate the model of the PMSM and controller a motor test bench was used. The motor test bench includes a load motor and a torque transducer for measuring shaft torque. A simulation model of the motor test bench was developed utilizing a similar spring-mass model of the mechanical system that is also used to model mechanics of the EMLA. It was found out that the simulation model of the motor test bench agrees well with the measurement data. Velocity and position tracking of the simulator presented the behavior of the real system with good accuracy. It was also found out that the controller uses different flux weakening algorithm compared to the simple algorithm chosen for modelling. To develop a model of the flux weakening algorithm used by the controller more testing would be required. However, the flux weakening algorithm is not very important when it come to this thesis as operating near the performance limits of the motor and controller was not of interest. This thesis provided information about different flux weakening algorithms if developing a model of better algorithm becomes necessary in the future. However, if the intention is to model the performance limits of the motor and controller, magnetic saturation should also be considered.

As the models for the PMSM and the control system were proven to be sufficiently accurate the model of the boom was then constructed. The boom model has a large part in common with the validated motor test bench model. The mechanical model of the actuator is very similar to the motor test bench mechanical model. The mechanical model of the boom itself was implemented using Simscape Multibody. A simple assumption of constant efficiency was used to form friction model for the actuator. The efficiency was determined from measurement data of the boom. The simulation results showed similar behavior to the real system. Both the simulator and real system showed poor control performance. The main problems are the oscillation in the speed of the motor and lag followed by jerk when accelerating from stand still. It was found out that problems occur due to low control loop frequency and delay in the control loop. The simulation model

was updated to correspond a system with servo drive intended for motion control applications. Both position and velocity tracking of the system improved significantly and the oscillation in speed vanished.

To improve the system's performance the motor and motor controller should be replaced. This should improve the control performance and make further studying of the EMLA more feasible. With better speed reference tracking a large set of good quality data could be collected to develop better experimental friction model for the actuator. The friction model used in this thesis is too inaccurate and developing a better one is necessary to improve the mechanical model. However, to develop a good friction model the load force of the actuator must be known accurately. Inaccuracy in the mass parameters of the boom and friction in the joints of the boom make it difficult to predict the load force accurately. A force sensor could be used to measure the load force directly. An even better alternative would be to construct a test bench for the actuator were the load force could be adjusted and measured accurately.

This thesis presented the theory behind modelling PMSM drive and mechanics of the EMLA. The models were found to be accurate enough to predict controllability issues of the system. The models can be used in future projects to study the systems before building prototypes. The models developed in this thesis form a good basis on developing improved models as studying electrification of mobile machines continues.

REFERENCES

[1]   International Energy Agency, "Electric Vehicles." https://www.iea.org/reports/electric-vehicles

[2]   Ponsse Studio, "Ponsse launches new technology: an electric forest machine," Aug. 17, 2022. https://www.ponsse.com/company/news/-/asset_publisher/P4s3zYhpxHUQ/content/ponsse-launches-new-technology-an-electric-forest-machine#/

[3]   Sandvik, "AUTOMINE® CONCEPT THE NEXT GENERATION OF AUTONOMOUS DRILLING." https://www.rocktechnology.sandvik/en/campaigns/nextgenautomation/

[4]   N. Mohan, *Advanced Electric Drives: Analysis, Control, and Modeling Using MATLAB/Simulink*, vol. 9781118485. John Wiley & Sons, Inc., 2014. doi: 10.1002/9781118910962.

[5]   R. Caracciolo and D. Richiedei, "Optimal design of ball-screw driven servomechanisms through an integrated mechatronic approach," *Mechatronics*, vol. 24, no. 7, pp. 819–832, Oct. 2014, doi: 10.1016/j.mechatronics.2014.01.004.

[6]   G. Ellis, *Control System Design Guide*. St. Louis: Elsevier Science & Technology, 2012. doi: 10.1016/C2010-0-65994-3.

[7]   C. Danielle, "What are coreless DC motors?, Motion Control Tips," 2018. https://www.motioncontroltips.com/what-are-coreless-dc-motors/

[8]   J. F. Gieras, *Permanent Magnet Motor Technology : Design and Applications*. CRC PRESS LLC, 2010.

[9]   N. Mohan, T. M. Undeland, and W. P. Robbins, *Power electronics - Converters, applications and design*. John Wiley & Sons, Inc., 2002. doi: 10.1016/s0026-2692(97)87859-7.

[10]   F. Giri, *AC Electric Motors Control: Advanced Design Techniques and Applications*. John Wiley & Sons, Inc., 2013. doi: 10.1002/9781118574263.

[11]   Werner. Leonhard, *Control of electrical drives*, 3rd ed. Berlin: Springer, 2001.

[12]   B. K. Bose, *Modern Power Electronics and AC Drives*. 2002.

[13]   M. Baradkar, "Slip ring Induction Motor, How it works?, Lesics," 2019. https://www.lesics.com/slip-ring-induction-motor-how-it-works.html

[14]   J. W. Schultz and S. Huard, "Comparing AC Induction with Permanent Magnet motors in hybrid vehicles and the impact on the value proposition © Copyright 2013 to the present , Parker Hannifin Corporation," 2015.

[15]   H. Heidari *et al.*, "A review of synchronous reluctance motor-drive advancements," *Sustain. Basel Switz.*, vol. 13, no. 2, pp. 1–37, 2021, doi: 10.3390/su13020729.

[16]   "IE5 synchronous reluctance motors, ABB," 2021. https://new.abb.com/news/detail/80775/ie5-synchronous-reluctance-motors

[17]   A. M. EL-Refaie, "Fractional-slot concentrated-windings synchronous permanent magnet machines: Opportunities and challenges," *IEEE Trans. Ind. Electron.*, vol. 57, no. 1, 2010, doi: 10.1109/TIE.2009.2030211.

[18]   P. Salminen, M. Niemela, J. Pyrhönen, and J. Mantere, "Performance analysis of fractional slot wound PM-motors for low speed applications," in *Conference Record of the 2004 IEEE Industry Applications Conference, 2004. 39th IAS Annual Meeting*, 2004, vol. 2, pp. 1032–1037 vol.2. doi: 10.1109/IAS.2004.1348540.

[19]   F. Magnussen, P. Thelin, and C. Sadarangani, "Performance evaluation of permanent magnet synchronous machines with concentrated and distributed windings including the effect of field-weakening," in *IEE Conference Publication*, 2004, vol. 2, pp. 679–685.

[20]   G. Pellegrino, T. M. Jahns, N. Bianchi, W. Soong, and F. Cupertino, *The Rediscovery of Synchronous Reluctance and Ferrite Permanent Magnet Motors*. 2016.

[21]   S. Filizadeh, *Electric machines and drives : principles, control, modeling, and simulation*, 1st edition. Boca Raton: CRC Press, Taylor & Francis Group, 2013.

[22]   P. Kundur, *Power System Stability and Control*. McGraw-Hill, 1994.

[23]   S. E. Lyshevski, *Electromechanical Systems and Devices*. CRC Press, 2008.

[24]   A. M. EL-Refaie and T. M. Jahns, "Optimal flux weakening in surface PM machines using fractional-slot concentrated windings," *IEEE Trans. Ind. Appl.*, vol. 41, no. 3, 2005, doi: 10.1109/TIA.2005.847312.

[25]   F. Meier and J. Soulard, "dq theory applied to a permanent magnet synchronous machine with concentrated windings," in *4th IET International Conference on Power Electronics, Machines and Drives (PEMD 2008)*, 2008, no. 538, pp. 194–198. doi: 10.1049/cp:20080510.

[26] S. Morimoto, M. Sanada, and Y. Takeda, "Effects and Compensation of Magnetic Saturation in Flux-Weakening Controlled Permanent Magnet Synchronous Motor Drives," *IEEE Trans. Ind. Appl.*, vol. 30, no. 6, 1994, doi: 10.1109/TIA.1994.350318.

[27] I. Hammoud, K. Xu, S. Hentzelt, T. Oehlschlaegel, and R. Kennel, "On offset-free continuous model predictive current control of permanent magnet synchronous motors," in *IFAC-PapersOnLine*, 2020, vol. 53, no. 2. doi: 10.1016/j.ifacol.2020.12.088.

[28] N. P. Quang and J. A. Dittrich, "Vector Control of Three-Phase AC Machines: System Development in the Practice," *Power Syst.*, vol. 20, 2008.

[29] N. Bianchi, P. G. Carlet, L. Cinti, and L. Ortombina, "A Review about Flux-Weakening Operating Limits and Control Techniques for Synchronous Motor Drives," *Energies*, vol. 15, no. 5. 2022. doi: 10.3390/en15051930.

[30] S. Morimoto, M. Sanada, and Y. Takeda, "Wide-Speed Operation of Interior Permanent Magnet Synchronous Motors with High-Performance Current Regulator," *IEEE Trans. Ind. Appl.*, vol. 30, no. 4, 1994, doi: 10.1109/28.297908.

[31] M. E. Haque, L. Zhong, and M. F. Rahman, "Improved trajectory control for an interior permanent magnet synchronous motor drive with extended operating limit," *J. Electr. Electron. Eng. Aust.*, vol. 22, no. 1, 2002.

[32] C. Maxfield, *Electrical engineering*, 1st edition. Amsterdam ; Newnes/Elsevier, 2008.

[33] M. Tursini, E. Chiricozzi, and R. Petrella, "Feedforward flux-weakening control of surface-mounted permanent-magnet synchronous motors accounting for resistive voltage drop," *IEEE Trans. Ind. Electron.*, vol. 57, no. 1, 2010, doi: 10.1109/TIE.2009.2034281.

[34] Z. Mihailovic, "Modeling and Control design of VSI-Fed PMSM drive systems with active load," Virginia Tech, 1998.

[35] T. M. Jahns, "Flux-weakening regime operation of an interior permanent-magnet synchronous motor drive," *IEEE Trans. Ind. Appl.*, vol. IA-23, no. 4, 1987, doi: 10.1109/TIA.1987.4504966.

[36] G. Scelba, G. De Donato, G. Scarcella, F. Giulii Capponi, and F. Bonaccorso, "Fault-tolerant rotor position and velocity estimation using binary hall-effect sensors for low-cost vector control drives," *IEEE Trans. Ind. Appl.*, vol. 50, no. 5, 2014, doi: 10.1109/TIA.2014.2304616.

[37] F. Giulii Capponi, G. De Donato, L. Del Ferraro, O. Honorati, M. C. Harke, and R. D. Lorenz, "AC brushless drive with low-resolution hall-effect sensors for surface-mounted PM machines," *IEEE Trans. Ind. Appl.*, vol. 42, no. 2, 2006, doi: 10.1109/TIA.2005.863904.

[38] S. Morimoto, M. Sanada, and Y. Takeda, "Sinusoidal current drive system of permanent magnet synchronous motor with low resolution position sensor," in *Conference Record - IAS Annual Meeting (IEEE Industry Applications Society)*, 1996, vol. 1. doi: 10.1109/ias.1996.556990.

[39] C. Miguel-Espinar, D. Heredero-Peris, G. Igor-Gross, M. Llonch-Masachs, and D. Montesinos-Miracle, "An enhanced electrical angle representation in PMSM control with misplaced Hall-effect switch sensors," in *23rd International Conference on Electrical Machines and Systems, ICEMS 2020*, 2020. doi: 10.23919/ICEMS50442.2020.9291194.

[40] P. B. Beccue, S. D. Pekarek, B. J. Deken, and A. C. Koenig, "Compensation for asymmetries and misalignment in a Hall-effect position observer used in PMSM torque-ripple control," *IEEE Trans. Ind. Appl.*, vol. 43, no. 2, 2007, doi: 10.1109/TIA.2006.889883.

[41] K. Kolano, B. Drzymała, and J. Gęca, "Sinusoidal control of a brushless dc motor with misalignment of hall sensors," *Energies*, vol. 14, no. 13, 2021, doi: 10.3390/en14133845.

[42] G. Wang, M. Valla, and J. Solsona, "Position sensorless permanent magnet synchronous machine drives - A review," *IEEE Trans. Ind. Electron.*, vol. 67, no. 7, 2020, doi: 10.1109/TIE.2019.2955409.

[43] I. Ansoategui and F. J. Campa, "Mechatronics of a ball screw drive using an N degrees of freedom dynamic model," *Int. J. Adv. Manuf. Technol.*, vol. 93, no. 1–4, 2017, doi: 10.1007/s00170-017-0597-2.

[44] Schaeffler Technologies GmbH & Company KG, *Schaeffler Technical Pocket Guide*. 2014.

[45] C. G. Zhou, H. T. Feng, Z. T. Chen, and Y. Ou, "Correlation between preload and no-load drag torque of ball screws," *Int. J. Mach. Tools Manuf.*, vol. 102, 2016, doi: 10.1016/j.ijmachtools.2015.11.010.

[46] Thomson Linear, "Ball Screws - Preloaded Nut." https://www.thomsonlinear.com/en/training/ball_screws/preloaded_nut

[47] M. Rigacci, R. Sato, and K. Shirase, "Experimental evaluation of mechanical and electrical power consumption of feed drive systems driven by a ball-screw," *Precis. Eng.*, vol. 64, 2020, doi: 10.1016/j.precisioneng.2020.04.016.

[48] D. Olaru, G. C. Puiu, L. C. Balan, and V. Puiu, "A new model to estimate friction torque in a ball screw system," in *Product Engineering: Eco-Design, Technologies and Green Energy*, 2005. doi: 10.1007/1-4020-2933-0_20.

[49] J. Sušeň, "A Study on the Ball Screw Friction Torque," *Stud. Conf. STC2011*, 2011.

[50] C. C. Wei, J. F. Lin, and J.-H. Horng, "Analysis of a ball screw with a preload and lubrication," *Tribol. Int.*, vol. 42, no. 11–12, pp. 1816–1831, Dec. 2009, doi: 10.1016/j.triboint.2008.12.013.

[51] L. C. Zhang and C. G. Zhou, "Experimental Study on the Coefficient of Friction of the Ball Screw," *J. Tribol.*, vol. 144, no. 3, 2022, doi: 10.1115/1.4051157.

[52] G. Ellis, *Control System Design Guide*. St. Louis: Elsevier Science & Technology, 2012. doi: 10.1016/C2010-0-65994-3.